*Desalination and Water Treatment*
www.deswater.com
doi: 10.5004/dwt.2023.29834

306 (2023) 131–150
September

# Porous carbon materials derived from biomass waste as efficient electrodes for capacitive deionization desalination

Wenquan Wang, Xiuwei Li*, Wanshi Zhang, Yan Wang*

*School of Energy and Power Engineering, Nanjing University of Science and Technology, Nanjing 210094, China, emails: good3000best@163.com (X. Li), YW2001@163.com (Y. Wang), 503061040@qq.com (W. Wang), good3000best@126.com (W. Zhang)*

Received 22 January 2023; Accepted 12 August 2023

**ABSTRACT**

The scarcity of freshwater has attracted the attention of countries around the world. Capacitive deionization (CDI) is a burgeoning green desalination technology with low price and high efficiency. The properties of the CDI electrodes directly affect the deionization efficiency. It is a hot spot of CDI technology research to develop electrode materials with higher adsorption capacity, better sustainability and lower cost. On this purpose, porous carbon materials derived from corncobs, cornstalks and waste cigarette butts have been firstly used as electrodes for CDI desalination in this paper. Eight derived materials have been successfully prepared through carbonization and activation. The morphology characteristics and electrochemical performance of the materials have been examined. Their desalination performance has been investigated. The results show corncobs activated at 800°C (CBC-800) have the best properties with a specific surface area of 1,201.9 $m^2 \cdot g^{-1}$ and pore size of 1.7268 nm. The CBC-800 electrode also possesses a high specific capacitance of 141.4 $F \cdot g^{-1}$ and low inner resistance. The salt adsorption capacity is 19.2 $mg \cdot g^{-1}$ and the charge efficiency is 60.3% in a 3,000 $mg \cdot L^{-1}$ NaCl solution at 1.2 V. CBC-800 is expected to be an efficient electrode material for CDI applications.

*Keywords:* Biomass waste; Porous carbon; Capacitive deionization; Desalination

## 1. Introduction

The shortage of freshwater is one of the most serious problems that needs to be solved, which is crucial for humans to survive: indeed, a person can only live for 3 d without water [1,2]. In addition, freshwater is an indispensable resource for developing a country's economy, especially in agriculture, industry and manufacturing [3]. About 3% of the world's water is freshwater. Meanwhile, approximately 70% of the world's freshwater is frozen in glaciers, which are difficult and costly to develop. The remaining 30% of the freshwater is exploitable groundwater [4,5]. However, the population explosion, economic development, water pollution and so on have led to severe freshwater storages all over the world [6]. For example, about 800 million people do not have clean water to drink and 2.5 billion people are exposed to severe health risks because there is no clean water [7]. Besides, the Covid-19 pandemic has caused a rapid increase in water consumption due to public health demands [2]. About 768 million people in the world lacked clean water 10 y ago, and 1.8 billion people by 2025 would face water storage. Demand for freshwater is expected to increase by 55% by 2050 as a result of population expansion and economic development [8,9]. Therefore, it needs the joint efforts of all countries in the world to solve the freshwater problem.

Seawater is the most abundant water resource in the world [10]. Roughly 75% of the earth's surface is covered with

* Corresponding author.

water, and 97% of it is seawater [11]. Unfortunately, seawater cannot be directly used by humans. If seawater can be turned into freshwater for human consumption, the shortage of freshwater will be solved. Traditional desalination technologies such as distillation, reverse osmosis, and electrodialysis are limited because of the frequent maintenance of the infrastructure and the high energy consumption during the operation [12–14]. Compared with traditional technologies, capacitive deionization (CDI) has received great concern due to its low price, green and high efficiency [15–18]. CDI is a burgeoning and potential desalination technology, which is based on reversible salt adsorption–desorption at carbon electrodes [19–21]. Research has been extensively carried out in the preparation of carbon materials, the improvement and mathematical modeling of CDI systems [22].

The theoretical basis of CDI is the electric double-layer (EDL) theory. The function of CDI system is achieved by supplying an external voltage that causes the ions to be absorbed on the surface of the carbon electrodes. As shown in Fig. S1, the traditional CDI system consists of a carbon electrode pair are separated by a flowing solution, including the deionization process and regeneration process. By applying a voltage, anions and cations in solution move to the positive and negative poles under the action of the electric field and are adsorbed into the EDL at the surface of the electrodes, respectively. After a while, a large number of ions are adsorbed on the surface of the electrodes so that the electrodes reach a saturated state. By shorting the positive pole and negative pole, the ions on the surface of the electrodes are released into the solution to form a salt solution, and the electrodes are correspondingly regenerated [23]. It can be seen that electrodes play an important role during the deionization and regeneration process. In general, a good CDI electrode material should have the following properties: a large ion-accessible specific surface area, excellent pore structure, high electronic conductivity, high electrochemical stability, and good regeneration ability [21].

At present, there have been many studies on CDI electrodes, such as the modification of traditional carbon materials and the development of new composite materials. Kim et al. [24] proposed a hierarchically open-porous nitrogen-incorporated carbon polyhedrons derived from metal–organic frameworks for improved CDI performance. Yan et al. [25] have made investigation on a sandwich-like nitrogen-doped graphene composites via a self-assembling strategy. However, the development of carbon materials for CDI desalination still has some difficulties [22,26–29]. For example, traditional carbon materials with large specific surface area (such as graphene, carbon nanotubes and so on) are limited due to high cost and complex preparation process [30–32]. Low-cost and abundantly available biochar through carbonization and chemical activation at high temperatures in an oxygen-free environment has low ion-accessible specific surface area and poor performance [34,35]. Therefore, the development of CDI electrode materials with high salt adsorption capacity still requires a lot of effort.

Biomass waste is cheap and easy to obtain, and it is a renewable resource. However, most biomass waste is discarded without being environmentally friendly, causing serious environmental pollution [36]. Park et al. [37,38] have made brilliant works on porous carbon materials derived from biomass to improve the performance of electrodes. In this paper, we prepared porous carbon materials derived from corncobs, cornstalks, and waste cigarette butts through carbonization and $K_2CO_3$ activation at high temperatures and developed as efficient electrodes for CDI desalination. The raw materials are cheap and easy to obtain, and the preparation method is green and convenient. Most biochar is modified with KOH, while green $K_2CO_3$ is selected as the activator in this paper. And no article has reported the research of corncobs for CDI desalination. The results show that the corncobs activated at 800°C (CBC-800) possess an excellent pore structure and the highest specific surface area of 1,201.9 $m^2 \cdot g^{-1}$. It has been demonstrated that the obtained electrode shows low inner resistance and the highest specific capacitance of 141.1 $F \cdot g^{-1}$ in a 1 M NaCl solution at a scan rate of 5 $mV \cdot s^{-1}$. The salt adsorption capacity of CBC-800 electrodes achieved 19.2 $mg \cdot g^{-1}$ in a 3,000 $mg \cdot L^{-1}$ NaCl solution and also exhibit a fast deionization rate, good regeneration behavior. This paper provides a reference for the reuse of biomass waste and the development of CDI electrodes.

## 2. Materials and methods

### 2.1. Preparation of biochar

Firstly, the corncobs were cleaned with deionized water and dried at 80°C for 12 h. The dried corncobs were then crushed into powder with a crusher. Secondly, the dried corncob powder was pre-carbonized at 400°C for 2 h (5°C·$min^{-1}$) under an $N_2$ atmosphere. The pre-carbonized powder was then washed with deionized water and dried at 80°C for 3 h. Thirdly, the black carbon powder was mixed with $K_2CO_3$ in a mortar (the ratio of carbon to $K_2CO_3$ is 1:5), and activated in a tube furnace at 700°C, 800°C or 900°C for 2 h under an $N_2$ atmosphere, respectively. A heating rate of 5°C·$min^{-1}$ was applied for the activation. Finally, the resulting black solid was washed with 10% HCl solution to remove the inorganic impurities and then washed with deionized water. The residue was collected and dried at 80°C for 3 h. The resultant porous carbon materials derived from corncobs are named CBC-X, where X indicates the activation temperature. Porous carbon materials derived from cornstalks and waste cigarette butts were prepared by the same method, named CS-X and WCB-X, respectively.

### 2.2. Characterization

All samples were observed by a scanning electron microscope (SEM, Hitachi SU8010) and transmission electron microscope (TEM, FEI Talos F200X). Textural properties of all samples were measured using a fully automatic surface area analyzer (BELSORP MAX) by nitrogen adsorption/desorption method, the specific surface area and the pore-size distribution of all samples were calculated based on Brunauer–Emmett–Teller (BET) and density functional theory (DFT), respectively. The crystal structure and defect degree were investigated by XRD diffractometer (Bruker D8 Advance) and Raman spectrometer (LabRAM HR Evolution). The elemental compositions were also analyzed by X-ray photoelectron spectroscopy (XPS) equipment (PHI Quantera II).

### 2.3. Electrochemical performance of carbon materials in 1 M NaCl solution

All electrochemical measurements were carried out with a CHI660D electrochemical workstation (Shanghai Chenhua Instruments Co.) at room temperature. In general, 10 wt.% acetylene black, 10 wt.% PTFE emulsion, and 80 wt.% porous carbon material were mixed and pressed onto a 1 $cm^2$ nickel foam. To ensure adequate mixing, a small amount of $C_2H_5OH$ can be added beforehand. The as-formed electrode was then dried at 80°C for 3 h in a vacuum oven. The quality of the active material on the electrode surface was calculated by the difference in weights before and after the coating of the samples. The as-prepared electrode was used as the working electrode in an electrochemical cell, while the Pt sheet and Ag/AgCl were used as the counter and reference electrodes, respectively. The specific capacitance ($C_{CV}$) was calculated from the cyclic voltammetry (CV) by the following formula [39]:

$$C_{CV} = \frac{\int IdV}{2mv\Delta V} \tag{1}$$

where $\int IdV$ is the area under the CV curve. $m$ is the weight of active material in the working electrode. $v$ is the scan rate. $\Delta V$ is the potential window.

The specific capacitance ($C_{GCD}$) was calculated from the galvanostatic charge/discharge (GCD) by the following formula [40]:

$$C_{GCD} = \frac{I\Delta t}{m\Delta V} \tag{2}$$

where $I$ is the current. $\Delta t$ is the discharge time. $m$ is the weight of active material in the working electrode. $\Delta V$ is the potential window.

### 2.4. Deionization experiments

The electrode slurry consists of 80 wt.% porous carbon material, 10 wt.% acetylene black, and 10 wt.% PTFE emulsion. The obtained slurry was pressed on a 28 $cm^2$ nickel foam. The as-formed electrode was then dried at 80°C for 3 h in a vacuum oven. Finally, the electrodes were equipped into the CDI unit to test the deionization performance. As shown in Fig. S2, the NaCl solution can flow through the CDI unit circularly with the help of the peristaltic pump. The electrochemical workstation can be used as a constant voltage source and records current. The conductivity meter can measure the conductivity of NaCl solution in real-time as a reflection of the change in solution concentration. Fig. S3 shows the structure of the CDI unit. The volume of NaCl solution is 100 mL. The concentrations of NaCl solution are 1,000; 2,000 and 3,000 $mg{\cdot}L^{-1}$. The charging voltages are 0.8–1.2 V.

The salt adsorption capacity (SAC) of the electrodes can be calculated using the following formula [41]:

$$\mathrm{SAC} = \frac{(C_0 - C_t)V}{m} \tag{3}$$

where $C_0$ and $C_t$ represent the start and end concentrations, respectively. $V$ is the solution volume. $m$ is the weight of active material.

The charge efficiency (η) can be achieved by the following equation [42]:

$$\eta = \frac{\mathrm{SAC} \times F}{\sum} \tag{4}$$

where $F$ is the Faraday constant (96,485 $C{\cdot}mol^{-1}$). $\sum$ is the amount of charge, which can be calculated by integrating the current.

## 3. Results and discussion

### 3.1. Characteristics

The activation temperature is an important factor that affects the properties of biochar. When the activation temperature exceeds 700°C, $K_2CO_3$ would decompose and a series of reactions would take place as indicated in Eqs. (5)–(8) [43].

$$K_2CO_3 \rightarrow K_2O + CO_2 \tag{5}$$

$$CO_2 + C \rightarrow 2CO \tag{6}$$

$$K_2CO_3 + 2C \rightarrow 2K + 3CO \tag{7}$$

$$C + K_2O \rightarrow 2K + CO \tag{8}$$

Fig. 2 shows the SEM image of biochar at different activation temperatures. Under the activation of $K_2CO_3$, as the activation temperature rises, the pore wall of the biochar becomes rough or even breaks and collapses, and the pores


Fig. 1. Schematic illustration of the preparation process of CBC.

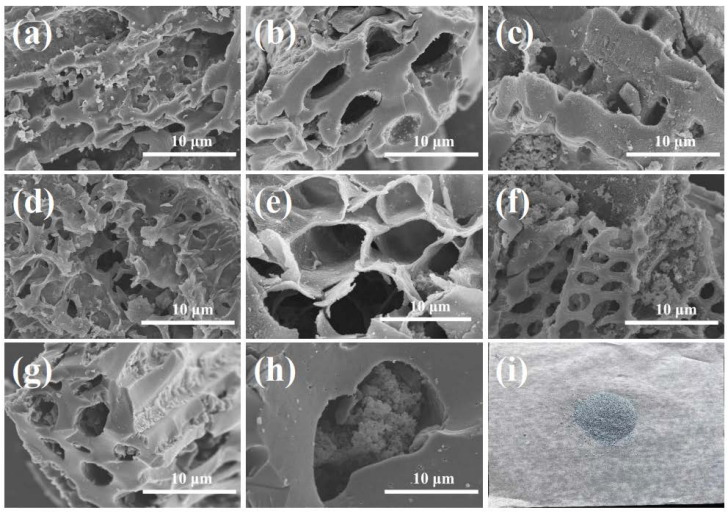


Fig. 2. Scanning electron microscope images of biochar: (a–c) CBC-X, (d–f) CS-X and (g–i) WCB-X.

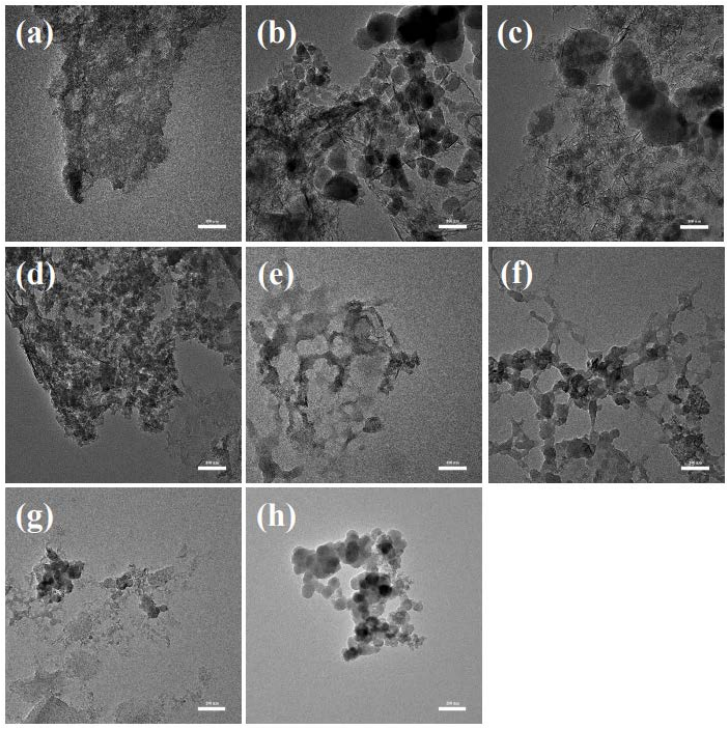


Fig. 3. Transmission electron microscope images of biochar: (a–c) CBC-X, (d–f) CS-X and (g–h) WCB-X.

are blocked. It is obvious that there are a large number of pores on the surface of CBC-800, CS-700 and WCB-800, and this dense pore structure provides conditions for the storage and transmission of ions. To further analyze the structure of carbon materials, TEM was used to characterize the biochar. As shown in Fig. 3, the carbon skeleton of all biochar was preserved after high-temperature activation. It is necessary to note that the activation reaction is more intense at high temperature. The higher the activation temperature, and the more intense the reaction. Different carbon materials have different densities. As shown in Fig. 2a, WCB-900 can be not prepared at 900°C due to WCB needs more $K_2CO_3$ in the activation process. So, the properties of WCB-900 are not discussed below.

Fig. 4 displays the nitrogen adsorption/desorption isotherms and pore-size distributions of CBC-X. According to the IUPAC Technical Report [44], the adsorption isotherm of CBC-700 has a large slope in the low-pressure region and there is almost no change in the medium-pressure region. It is inferred that the adsorption isotherm of CBC-700 belongs to the type-I curve. The adsorption isotherm of CBC-800 has a hysteresis loop, the adsorption branch

of the hysteresis loop is parallel to the desorption branch. It is inferred that the adsorption isotherm of CBC-800 is a typical type-IV curve with the type H4 hysteresis loop. The adsorption isotherm of CBC-900 is also a typical type-IV curve with the type H4 hysteresis loop. In addition, the pore size of CBC-700 is distributed in the range of 0~1 nm, indicating that CBC-700 is mainly microporous. The pore size of CBC-800 is distributed in the range of 0~2 nm, indicating that CBC-800 contains a large number of micropores and a small number of mesopores. The peak of the pore-size distribution curve of CBC-900 is 2 nm, indicating that CBC-900 is mainly mesoporous.

As shown in Fig. 5a, the adsorption isotherm of CS-700 and CS-800 have a large slope in the low-pressure region and there is almost no change in the medium-pressure region. It is inferred that the adsorption isotherm of CS-700 and CS-800 belong to the type-I curve. The adsorption isotherm of CS-900 has a hysteresis loop, the adsorption branch of

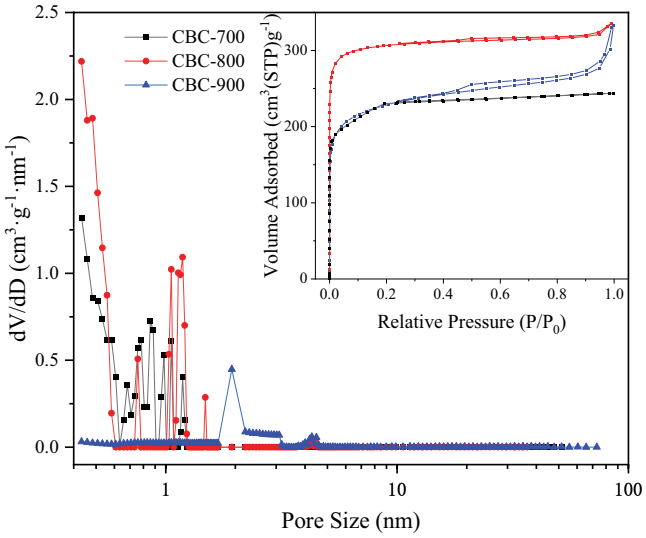


Fig. 4. Nitrogen sorption isotherms and pore-size distribution curves of CBC-X.

the hysteresis loop is parallel to the desorption branch. It is inferred that the adsorption isotherm of CS-900 is a typical type-IV curve with the type H4 hysteresis loop. Similarly, as shown in the inset of Fig. 5b, the adsorption isotherm of WCB-700 and WCB-800 belong to the type-I curve. But the adsorption isotherm of WCB-X has an obvious unclosed hysteresis loop. This hysteresis loop is not proof of the type-IV curve. Instead, nitrogen has a chemical reaction with some substances in the material, so that the adsorption branch and the desorption branch are not closed.

Table 1 shows the test results of the specific surface area analyzer of all samples. The specific surface area, total pore volume and average pore size of CBC-700 are 825.32 $m^2 \cdot g^{-1}$, 0.3771 $cm^3 \cdot g^{-1}$ and 1.8277 nm, respectively. The specific surface area, total pore volume and average pore size of CBC-800 are 1,201.90 $m^2 \cdot g^{-1}$, 0.5188 $cm^3 \cdot g^{-1}$ and 1.7268 nm, respectively. The specific surface area, total pore volume and average pore size of CBC-900 are 853.60 $m^2 \cdot g^{-1}$, 0.4830 $cm^3 \cdot g^{-1}$ and 2.2624 nm, respectively. When the activation temperature increases from 700°C to 800°C, the specific surface area and total pore volume of CBC-X increase, but the average pore size decreases. On one hand, as the activation temperature increases, the chemical reaction between the activator and the biochar is intensified, which increases the pore of the biochar. On the other hand, the area of biochar is constant. If the pores on the carbon

Table 1
Pore characteristics of porous carbon materials

| Samples | $S_{BET}$ ($m^2 \cdot g^{-1}$) | $V_{total}$ ($cm^3 \cdot g^{-1}$) | $D_{ave}$ (nm) |
|---|---|---|---|
| CBC-700 | 825.32 | 0.3771 | 1.8277 |
| CBC-800 | 1,201.90 | 0.5188 | 1.7268 |
| CBC-900 | 853.60 | 0.4830 | 2.2624 |
| CS-700 | 979.70 | 0.4692 | 1.9158 |
| CS-800 | 1,065.10 | 0.8606 | 3.2321 |
| CS-900 | 701.01 | 0.6612 | 3.7730 |
| WCB-700 | 428.25 | 0.2041 | 1.9064 |
| WCB-800 | 936.22 | 0.4065 | 1.7367 |

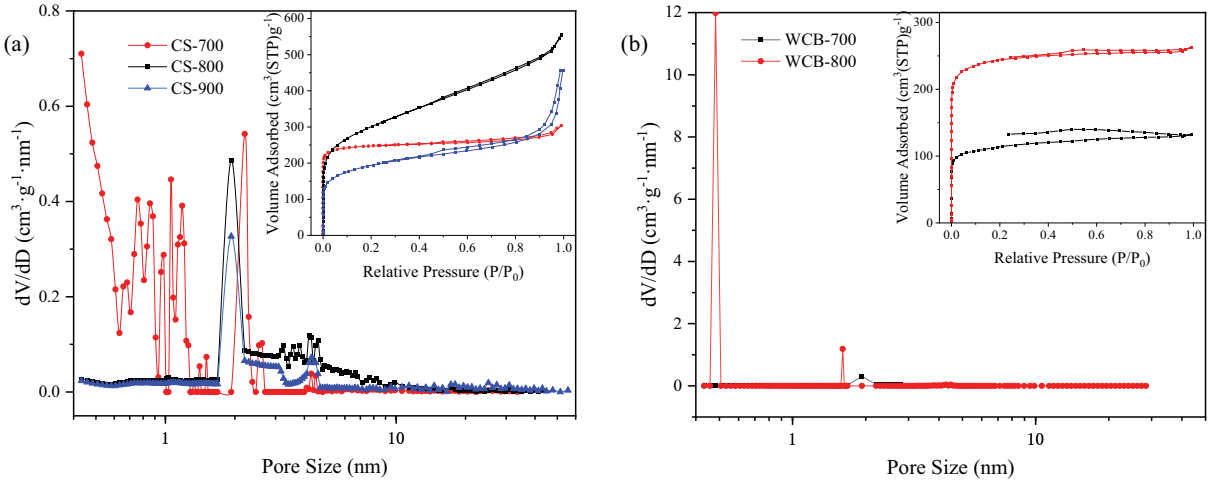


Fig. 5. Nitrogen sorption isotherms and pore-size distribution curves of biochar. (a) CS-X and (b) WCB-X.

surface increase, the diameter of the individual pores will decrease. When the activation temperature continues to increase to 900°C, the specific surface area and pore volume of CBC-X decrease. This is because the pore wall breaks and collapses, causing the small pore to be blocked or multiple small pores that have been formed into a large pore. The test results show that 800°C is the appropriate activation temperature for CBC-X, CS-X and WCB-X.

X-ray diffraction (XRD) is a common method to study the crystallinity and purity of carbon materials. Fig. 6a displays the XRD results of CBC-X, it can be seen that CBC-X possess an obvious graphitic stacking peak at 23° and a weak peak at 44°, which were considered as (002) and (100) planes of the carbon, respectively, indicating that the main component of the samples is amorphous carbon [45]. In addition, no other peaks can be seen, indicating that the purity of the samples is high. Raman is a common method to study the defect degree of carbon materials. Fig. 6b displays the Raman profiles of CBC-X, the peaks are located at about 1,350 and 1,580 $cm^{-1}$, corresponding to the D band and G band, respectively. The D band reflects amorphous carbon and defect structure and the G band reflects the ordered graphitic structure of $sp^2$ hybridization. The ratio of the D band to the G band ($I_D/I_G$) is used to characterize the defect degree of the sample [46]. The $I_D/I_G$ of CBC-700, CBC-800 and CBC-900 are 0.92, 0.94 and 0.34, respectively. It is proved that at an activation temperature of 800°C, $K_2CO_3$ makes the corncobs produce more pores, which is conducive to the storage and transmission of ions.

Similarly, as shown in Fig. 7, the $I_D/I_G$ of CS-700, CS-800 and CS-900 are 0.93, 0.95 and 0.67, respectively, the $I_D/I_G$ of WCB-700 and WCB-800 are 0.93 and 0.99, respectively. It is proved that 800°C is the appropriate activation temperature for CS-X and WCB-X.

To intensively explore the chemical compositions of the carbon materials, XPS analysis was performed. Figs. 8 and S4. show the content of C, N and O in CBC-X and its chemical state, the specific results are shown in Table 2. Oxygen could enhance the hydrophilicity and specific capacitance of biochar, nitrogen is assumed to be the main configuration contributing to the electrical conductivity and pseudo-capacitance of biochar. In addition, N-6 and C=O functional groups can work together to improve the specific capacitance of carbon materials [47–49]. Obviously, CBC-X has the highest nitrogen content, and N-6 accounts for 49.3%, while C=O accounts for 43.1% of oxygen. Under their joint action, CBC-800 will have the highest specific capacitance.

It is worth noting that the nitrogen content in CS-700 is higher, and the proportion of C=O is also very high. CS-700 may have the highest specific capacitance.

### 3.2. Electrochemical performance

The electrochemical behavior of biochar was carried out by cyclic voltammetry (CV), galvanostatic charge/discharge (GCD), and electrochemical impedance spectroscopy (EIS) measurements in a 1 M NaCl solution at room temperature. Fig. 10. depicts the CV profiles of CBC-X electrodes at a scan rate of 5 $mV \cdot s^{-1}$, all profiles have no oxidation and reduction peak, indicating an ideal electrochemical double-layer capacitance (EDLC) behavior between the solution and electrode rather than faraday reaction [50]. In addition, all profiles are symmetrical and almost rectangular shape, indicating the electrodes can realize ions adsorption and desorption rapidly [51]. According to Eq. (1), the specific capacitance of the CBC-700, CBC-800 and CBC-900 electrodes is 114.1, 141.4 and 75.0 $F \cdot g^{-1}$, respectively.

Similarly, the electrochemical behavior of CS-X electrodes is similar to that of CBC electrodes (Fig. 11a). The specific capacitance of the CS-700 electrode is 132.0 $F \cdot g^{-1}$, which is higher than the CS-800 and CS-900 electrodes (106 and 24.7 $F \cdot g^{-1}$, respectively). This is probably because the heteroatom content of CS-700 is higher than that of CS-800. However, the CV profiles of the WCB electrodes are extremely irregular (Fig. 11b), which is the result of the oxidation–reduction reaction of the nitrogen group. The specific capacitance of WCB-700 and WCB-800 is 58.6 and 76.4 $F \cdot g^{-1}$, respectively. We find that the CV profiles of CBC-X and WCB-X have a potential window of 0~–1.0 V, while the CV profiles of CS-X have a potential window of –0.2~–1.0 V. This is because the potential window of 0~1.0 V is large for CS-X. In this case, the migration rate and decomposition

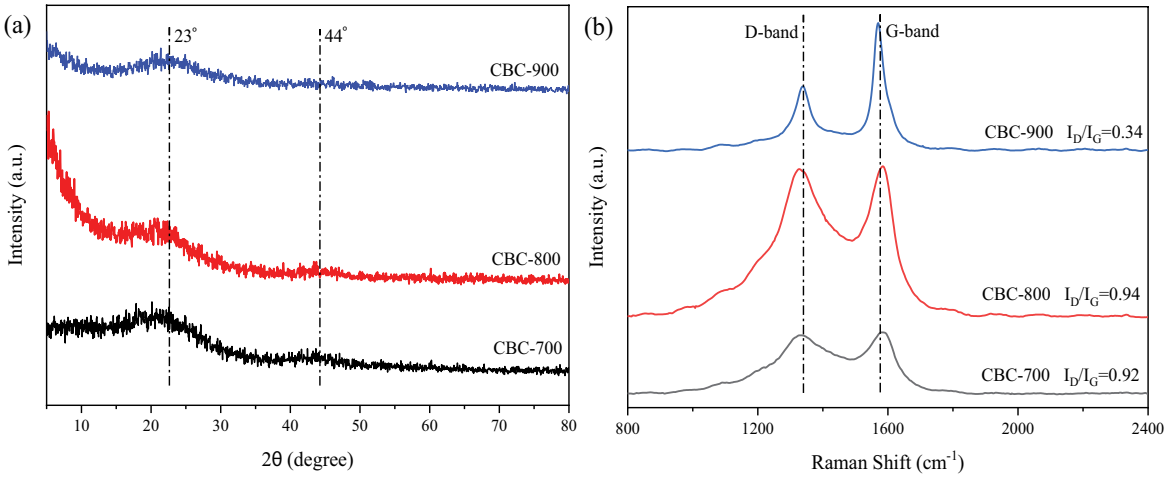


Fig. 6. (a) X-ray diffraction patterns and (b) Raman spectra of CBC-X.

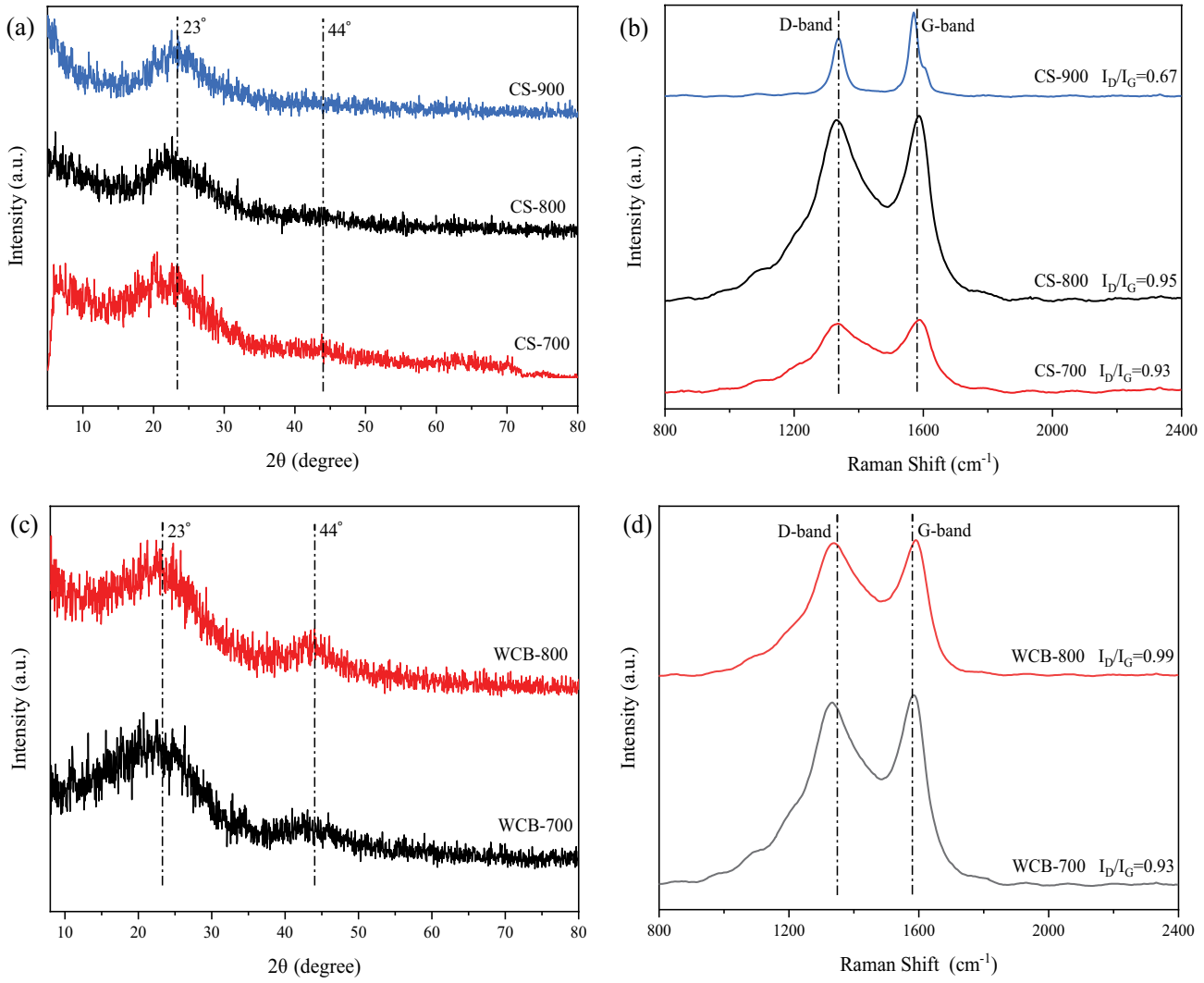


Fig. 7. (a) X-ray diffraction patterns and (b) Raman spectra of CS-X, (c) X-ray diffraction patterns and (d) Raman spectra of WCB-X.

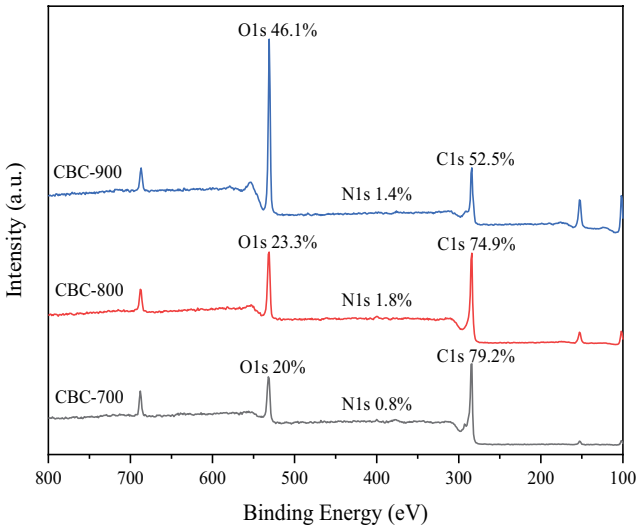


Fig. 8. Content of C, N and O elements for CBC-X.

rate of ions on the electrode surface are very fast, and the polarization phenomenon is easy to occur. Therefore, the high potential should be reduced so that the potential window becomes smaller. Overall, the highest specific capacitance of the CBC-800 electrode due to the excellent meso/microporous structure, higher specific surface area and the content of the N element. The specific capacitance of all carbon electrodes by CV tests at different scan rates from Eq. (1) is calculated in Table 3. Moreover, the CV curves of all carbon electrodes at different scan rates in a 1 M NaCl solution are shown in Fig. S7–S9.

Fig. 12 shows the GCD profiles of CBC-X electrodes at a current density of 0.25 $A \cdot g^{-1}$, all profiles show a triangular shape, indicating an ideal EDLC behavior rather than faraday reaction [52,53]. The discharge time of the CBC-800 electrode is longer than CBC-700 and CBC-900 electrodes, indicating that the CBC-800 electrode has higher specific capacitance, which is consistent with the CV results. However, the GCD profiles are not regular triangular, this is mainly because of the contact resistance between the

Table 2
Content of C, N and O elements of porous carbon materials

| Samples | C (%) | N (%) | | | O (%) | | |
|---|---|---|---|---|---|---|---|
| | | N-5 (%) | N-6 (%) | N-Q (%) | O-I (%) | O-II (%) | O-III (%) |
| CBC-700 | 79.2 | 0.8 | | | 20 | | |
| | | 37.2 | 48.6 | 14.2 | 38.5 | 27.8 | 33.7 |
| CBC-800 | 74.9 | 1.8 | | | 23.3 | | |
| | | 23.7 | 49.3 | 27 | 43.1 | 34.8 | 22.1 |
| CBC-900 | 52.5 | 1.4 | | | 46.1 | | |
| | | 45.6 | 29.8 | 24.6 | 34.3 | 59.1 | 6.6 |
| CS-700 | 68.6 | 1.2 | | | 30.2 | | |
| | | 30.6 | 46.7 | 22.7 | 42.9 | 32.1 | 25 |
| CS-800 | 67.1 | 0.3 | | | 32.6 | | |
| | | 32.2 | 44.2 | 23.6 | 36.7 | 30.9 | 32.4 |
| CS-900 | 59.8 | 0.1 | | | 40.1 | | |
| | | 39.5 | 54 | 6.5 | 31.7 | 55 | 13.3 |
| WCB-700 | 81 | 0.2 | | | 18.8 | | |
| | | 39.2 | 35.8 | 25 | 39.3 | 43.7 | 17 |
| WCB-800 | 76.9 | 0.9 | | | 22.2 | | |
| | | 31.9 | 31.1 | 37 | 41.9 | 34.7 | 23.4 |

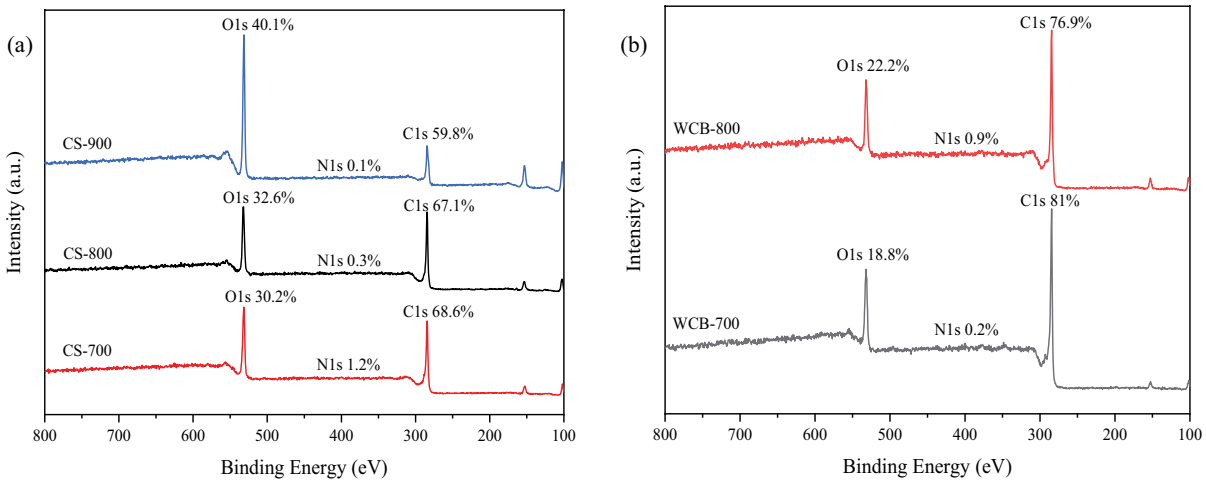


Fig. 9. Content of C, N and O elements of biochar. (a) CS-X and (b) WCB-X.

electrodes and salt solution [54]. For example, the IR drop at the start of discharge profile reflects the resistance of the solution-electrode interface. According to Eq. (2), the specific capacitance of CBC-700, CBC-800 and CBC-900 electrodes is 165, 180 and 54 $F \cdot g^{-1}$.

Likewise, the discharge time of the CS-700 electrode is longer than CS-800 and CS-900 electrodes (Fig. 13a), suggesting that the CS-700 electrode has higher specific capacitance, which is consistent with the CV results. The specific capacitance of the CS-700 electrode is 134.8 $F \cdot g^{-1}$, which is higher than the CS-800 (111 $F \cdot g^{-1}$) and CS-900 (32.7 $F \cdot g^{-1}$) electrodes. However, the GCD profiles of the WCB electrodes are extremely irregular due to the existence of the nitrogen element (Fig. 13b). The specific capacitance of WCB-700 and WCB-800 is 72.8 and 77.8 $F \cdot g^{-1}$, respectively. The GCD results demonstrate that the CBC-800 electrode has a more suitable pore structure for the storage and transport of ions. The specific capacitance of all carbon electrodes by GCD tests at different current densities from Eq. (2) is calculated in Table 4. In addition, the GCD curves of all carbon electrodes at different current densities in a 1M NaCl solution are shown in Figs. S7–S9.

To further evaluate the electrochemical behavior and electrical resistance by EIS. As shown in Fig. 14, the Nyquist plots of all carbon electrodes are composed of a semicircle in a high-frequency range and a slop line in a low-frequency range. In the high-frequency range, the diameter of the semicircle indicates the charge transfer resistance between the electrodes and solution. The $x$-intercept presents the equivalent series resistance (ESR), which reflects the

electrode resistance, charge transfer resistance, and contact resistance between the carbon materials and current collectors [55,56]. In the low-frequency range, the slope of the line represents the capacitive behaviors of the electrode. In Fig. 17, the charge transfer resistance of the CBC-700, CBC-800 and CBC-900 electrodes are 0.91, 0.92 and 0.8 Ω, respectively. Such a small value indicates that the charge transfer resistance of the CBC electrodes can be ignored. The ESR

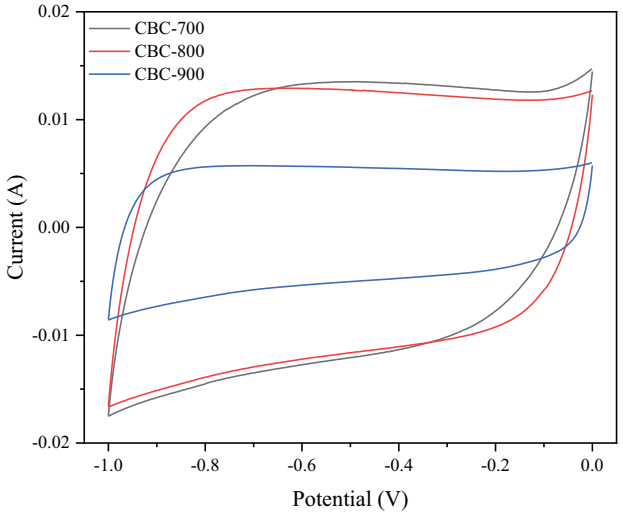


Fig. 10. Cyclic voltammetry (CV) curves of CBC-X electrodes in a 1 M NaCl solution at a scan rate of 5 mV·s$^{-1}$.

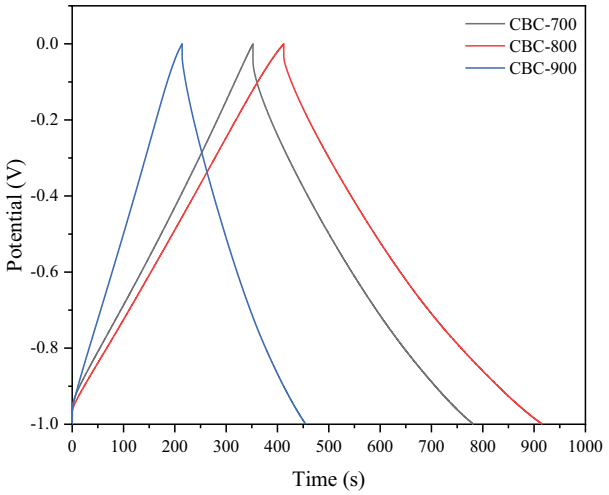


Fig. 12. Galvanostatic charge/discharge (GCD) curves of CBC-X electrodes in a 1 M NaCl solution at a current density of 0.25 A·g$^{-1}$.

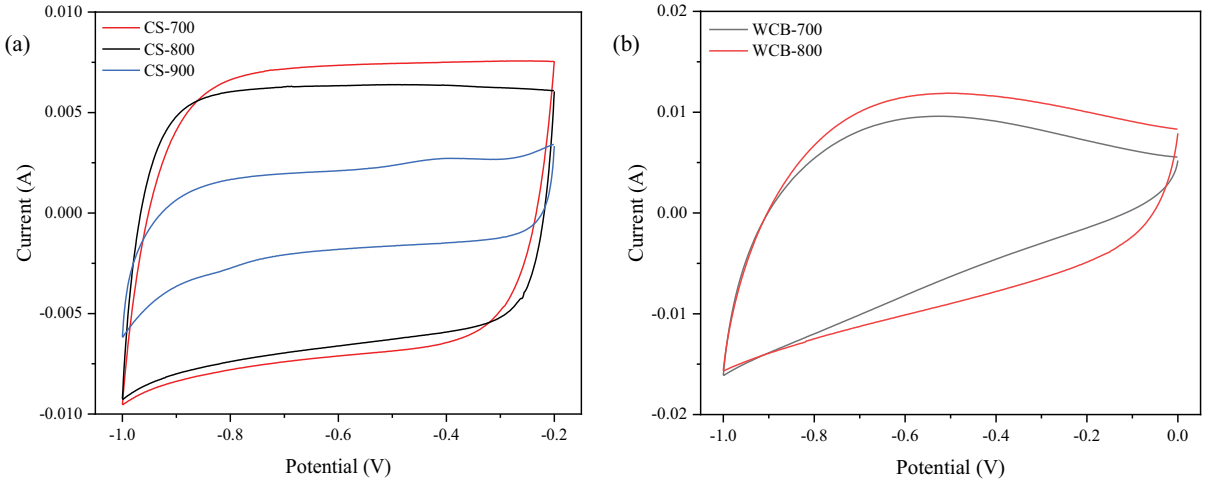


Fig. 11. CV curves of (a) CS-X and (b) WCB-X electrodes in a 1 M NaCl solution at a scan rate of 5 mV.

Table 3
Specific capacitance of all carbon electrodes with CV tests

| Samples | 5 mV·s$^{-1}$ | 10 mV·s$^{-1}$ | 20 mV·s$^{-1}$ | 50 mV·s$^{-1}$ | 75 mV·s$^{-1}$ | 100 mV·s$^{-1}$ |
|---|---|---|---|---|---|---|
| CBC-700 | 114.1 | 92.4 | 67.9 | 27.4 | 16.6 | 11.4 |
| CBC-800 | 141.4 | 120.7 | 89.8 | 47.5 | 31.3 | 22.0 |
| CBC-900 | 75.0 | 65.8 | 58.7 | 34.5 | 22.6 | 15.5 |
| CS-700 | 132.0 | 113.0 | 85.4 | 36.8 | 21.0 | 13.4 |
| CS-800 | 106.0 | 96.0 | 80.0 | 44.6 | 28.8 | 20.0 |
| CS-900 | 24.7 | 22.6 | 20.4 | 16.6 | 14.5 | 9.7 |
| WCB-700 | 58.6 | 38.7 | 23.9 | 9.7 | 6.3 | 4.9 |
| WCB-800 | 76.4 | 52.7 | 38.3 | 16.3 | 10.4 | 7.6 |

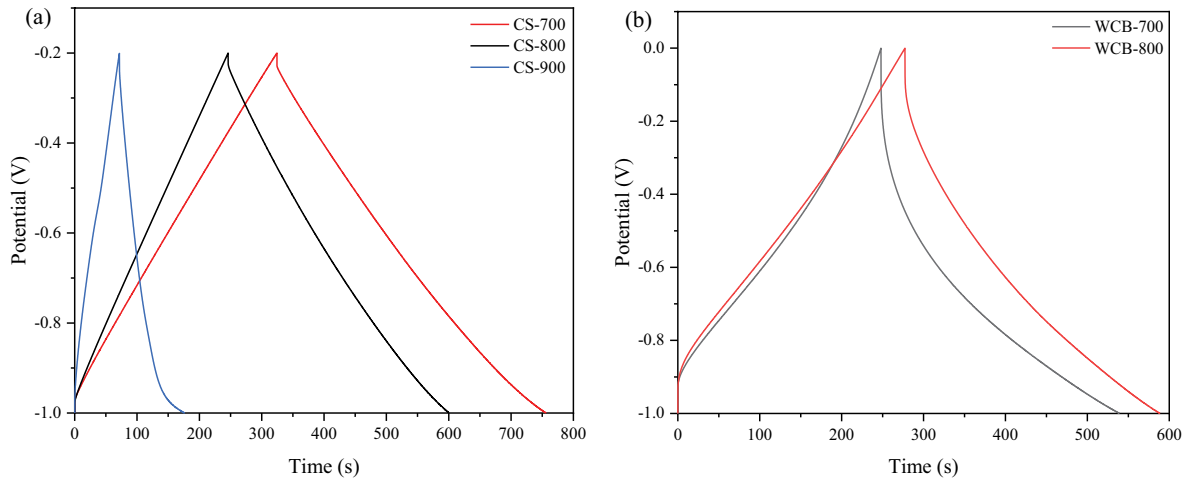


Fig. 13. GCD curves of (a) CS-X and (b) WCB-X electrodes in a 1 M NaCl solution at a current density of 0.25 A·g$^{-1}$.

Table 4
Specific capacitance of all carbon electrodes with GCD tests

| Samples | 0.25 A·g$^{-1}$ | 0.5 A·g$^{-1}$ | 0.75 A·g$^{-1}$ | 1.0 A·g$^{-1}$ |
|---|---|---|---|---|
| CBC-700 | 107.4 | 89.4 | 77.0 | 67.4 |
| CBC-800 | 126.1 | 110.5 | 100.9 | 93.2 |
| CBC-900 | 60.2 | 52.6 | 48.4 | 44.7 |
| CS-700 | 134.8 | 115.2 | 105.4 | 98.5 |
| CS-800 | 111.0 | 93.0 | 85.2 | 79.7 |
| CS-900 | 32.7 | 21.3 | 18.0 | 16.5 |
| WCB-700 | 72.8 | 51.8 | 39.2 | 29.0 |
| WCB-800 | 77.8 | 52.5 | 44.2 | 33.4 |

value of the CBC-700 electrode is 2.50 Ω, the ESR value of the CBC-800 electrode is 2.25 Ω, and the ESR value of the CBC-900 electrode is 3.27 Ω. The lower ESR of the CBC-800 electrodes can be attributed to the following reasons: On one hand, the meso/microporous structure is beneficial to ion storage and transfer, which can reduce the contact resistance between the electrodes and solution. On the other hand, the higher content of the N element leads to better electronic conductivity. The plot of the CBC-800 electrode has the highest slope, indicating it is a double electric layer adsorption and faster ions transport.

In Fig. 15a the ESR value of the CS-800 electrode is 3.30 Ω, which is lower than the CS-700 electrode (3.80 Ω) and CS-900 electrode (4.37 Ω). In Fig. 15b the ESR value of the WCB-700 and WCB-800 electrodes are 3.30 and 2.95 Ω, respectively. In brief, the CBC-800 electrode may have a good deionization ability due to its outstanding properties and electrochemical performance. The next step will be to explore the actual deionization ability of CBC, CS and WCB electrodes by experiments.

In particular, according to electrochemical results, the cycle stability of the CBC-800 electrode is measured by GCD. As shown in Fig. 16, the capacitance retention rate of the CBC-800 electrode is still close to 100% after 1,000 charge/discharge. Indicating that the CBC-800 electrode possesses excellent electrochemical stability and uses time longer.

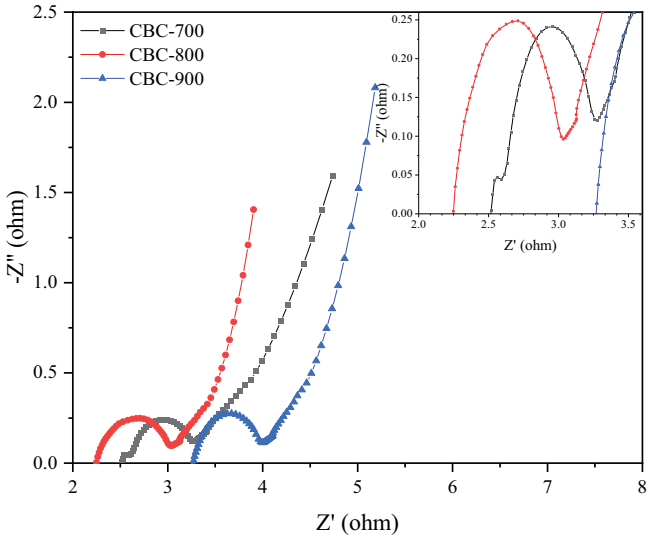


Fig. 14. Electrochemical impedance spectra (EIS) of CBC-X electrodes in a 1 M NaCl solution.

### 3.3. Deionization performance

The deionization ability of the CBC-X, CS-X and WCB-X electrodes was carried out in a 3,000 mg·L$^{-1}$ NaCl solution. As shown in Fig. 17a, the ion adsorption capacity of all electrodes increases rapidly within 5 min when 1.2 V voltage is applied and then stabilized after 15 min, indicating the electrodes reach saturation point within 15 min. The plot of the CBC-800 electrodes is steeper than other electrodes, indicating the adsorption rate of the CBC-800 electrodes is faster. After 15 min, the CBC-800 electrodes show the highest adsorption capacity, which reaches 19.2 mg·g$^{-1}$. As shown in Fig. S10a, the solution conductivity decreases within 600 s and then plateaued after 900 s, indicating the deionization process was completed within 900 s. The salt adsorption capacity of all carbon electrodes from Eq. (3) is calculated in Table 5. The highest salt adsorption capacity and fast adsorption rate of CBC-800 electrodes can be explained by the following aspects: The CBC-800 possesses

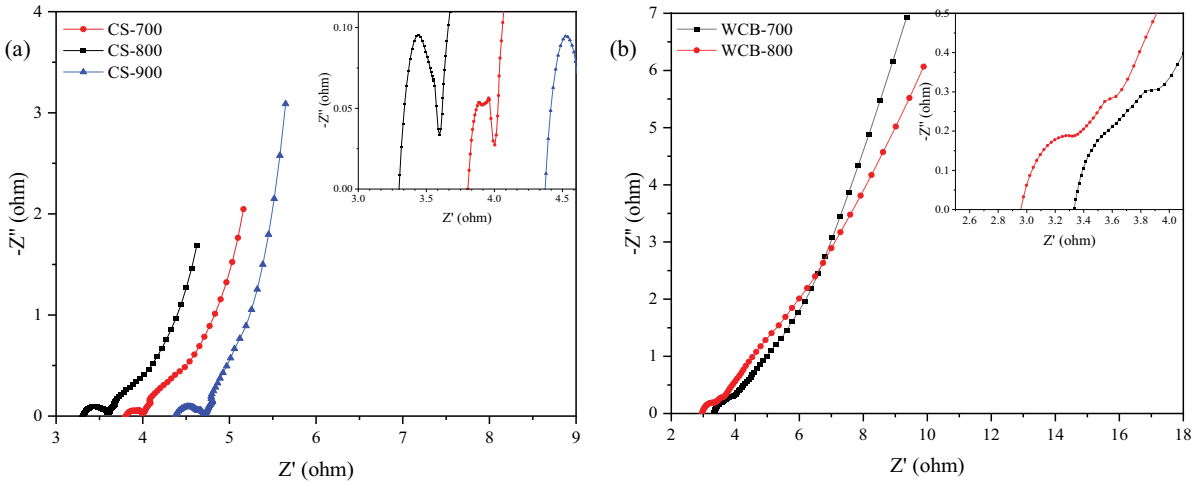


Fig. 15. EIS of (a) CS-X and (b) WCB-X electrodes in a 1 M NaCl solution.

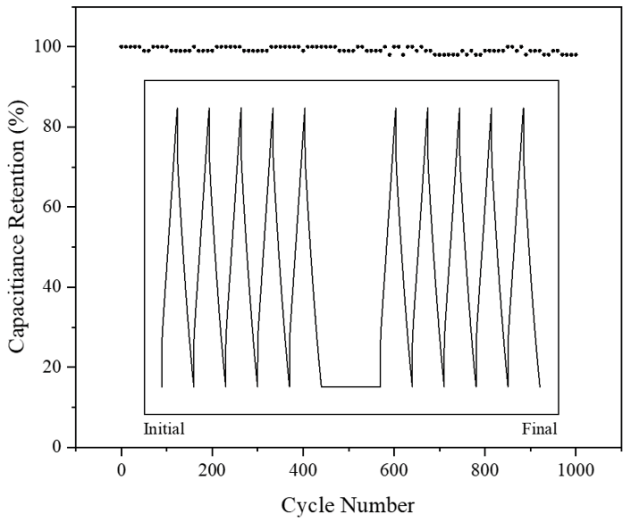


Fig. 16. Capacitance retention rate of the CBC-800 electrode by GCD at 1 A·g$^{-1}$.

the highest specific surface area and more pores consisting of micropores and mesopores. The micropores can provide more storage space for ions, and the mesopores can reduce the transport resistance of ions. In addition, the existence of the N element can create more defects, which favors ion diffusion and improves the electronic conductivity of carbon materials. Of course, too much or too little electrode slurry will affect the salt adsorption capacity of the CDI electrode. Because too little electrode slurry cannot be coated with the whole nickel foam, and too much electrode slurry will affect the performance of the internal slurry. The slurry quality of the single electrode in this paper is 350 mg, it is necessary to explore the influence of the quality of the electrode slurry on the salt adsorption capacity of electrode under the condition that the nickel foam can be coated. In a word, the CBC-800 electrodes show the best deionization ability due to its unique properties. Moreover, Figs. S11a and S12a show the solution conductivity changes for CS and WCB electrodes, respectively.

To explore the impact of the charging voltage on the deionization ability, the voltage of 0.8–1.2 V was used in the deionization experiments with CBC-800 electrodes in a 3,000 mg·L$^{-1}$ NaCl solution. As shown in Fig. 17b, once the charging voltage was applied, the SAC increases rapidly. When the voltage increases, the upward trend of electrosorption capacity is more obvious, indicating better SAC under the higher voltage. Generally, the increase of charging voltage can enhance the electric field intensity between the electrodes, which is beneficial to ion migration. Nevertheless, the charging voltage is always under 1.23 V, because hydrolytic reactions could appear at high voltage. The SAC of CBC-800 electrodes increased from 10.8 to 19.2 mg·g$^{-1}$ when the charging voltage increased from 0.8 to 1.2 V.

The effect of the initial NaCl concentration on the deionization performance was also studied. As shown in Fig. 17c, the higher solution concentration results in a higher SAC. The SAC of CBC-800 electrodes increased from 11.6 to 19.2 mg·g$^{-1}$ when the concentration of NaCl solution increased from 1,000 to 3,000 mg·L$^{-1}$. This could be explained by the following reasons: (i) The higher concentration provides more ions, which could reduce the difficulty of the electrodes to adsorb ions; (ii) The concentration of the solution increasing results in the faster formation of EDL, which facilitates the adsorption of ions. Compared with the activated carbon obtained through non-renewable energy (The adsorption capacity is 9.72 mg·g$^{-1}$ in 500 mg·L$^{-1}$ NaCl solution), CBC-800 also has a comparative power [57].

To investigate the regeneration behavior of CBC-800 electrodes, the cyclic salt adsorption–desorption experiments were conducted in a 3,000 mg·L$^{-1}$ NaCl solution at a charging voltage of 1.2 V and discharge voltage of 0 V. As shown in Fig. 17d, the solution conductivity dropped rapidly in 10 min when the voltage was applied. The solution conductivity increases and back to the initial value in 10 min when the voltage was stopped. If the performance of the electrode is poor, the time will be longer, but no more than 15 min. Of course, the size and quantity of electrodes

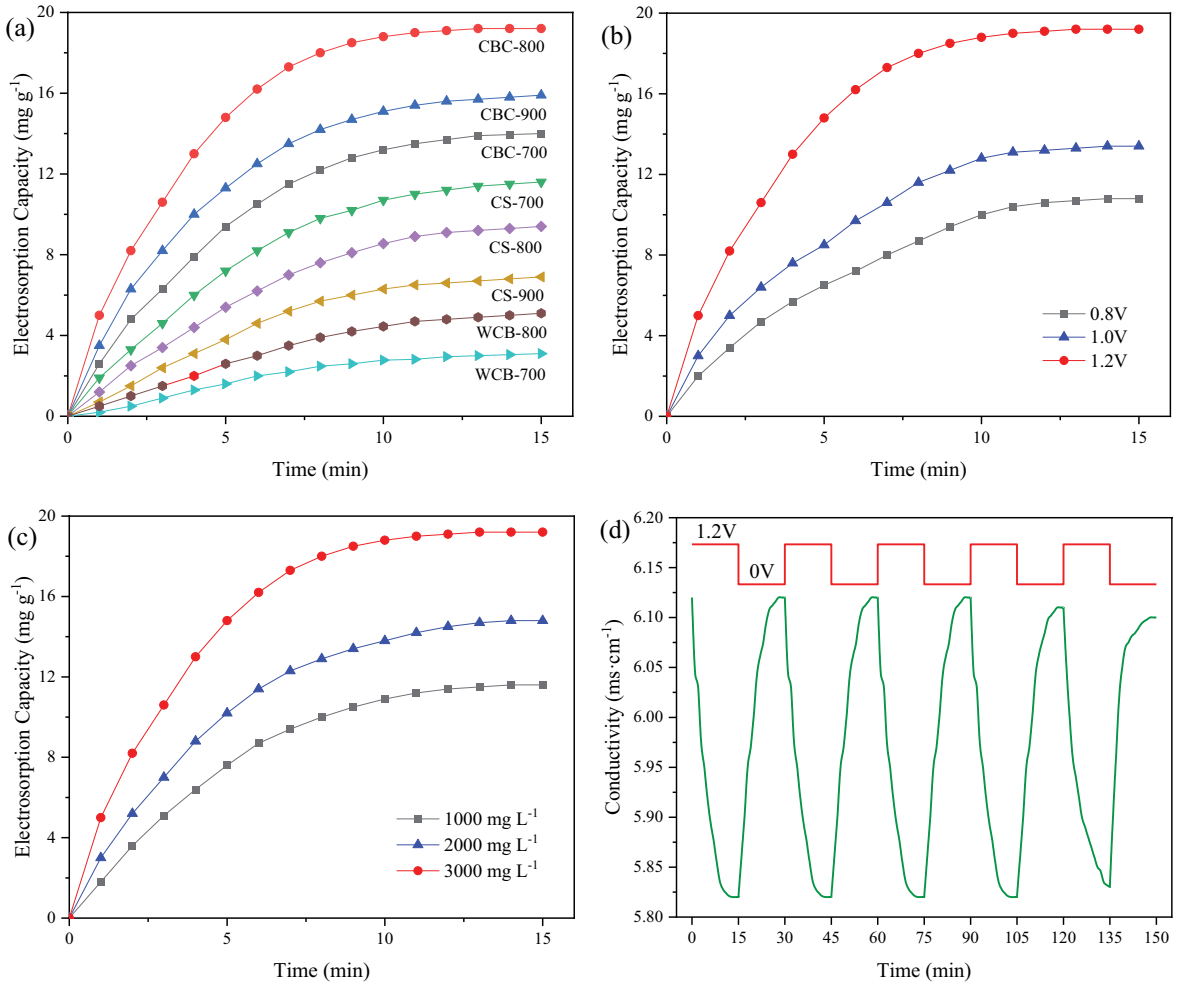


Fig. 17. (a) Plots of SAC vs. deionization time for the carbon electrodes in a 3,000 mg·L$^{-1}$ NaCl solution at 1.2 V. (b) Plots of SAC vs. deionization time for CBC-800 electrodes in a 3,000 mg·L$^{-1}$ NaCl solution at 0.8–1.2 V. (c) Plots of SAC vs. deionization time for CBC-800 electrodes at 1.2 V in a 1,000–3,000 mg·L$^{-1}$ NaCl solution. (d) Deionization–regeneration curves for CBC electrodes in a 3,000 mg·L$^{-1}$ NaCl solution at 1.2 V.

Table 5
SAC of biochar electrodes in different solution concentrations at 1.2 V

| Electrodes | 1,000 mg·L$^{-1}$ | 2,000 mg·L$^{-1}$ | 3,000 mg·L$^{-1}$ |
|---|---|---|---|
| CBC-700 | 9.3 | 11.6 | 14 |
| CBC-800 | 11.6 | 14.8 | 19.2 |
| CBC-900 | 8.5 | 10.8 | 15.9 |
| CS-700 | 7.8 | 8.7 | 11.6 |
| CS-800 | 5.6 | 6.8 | 9.4 |
| CS-900 | 2.5 | 4.6 | 6.9 |
| WCB-700 | 1.5 | 2.3 | 3.1 |
| WCB-800 | 3.6 | 4.1 | 5.1 |

will affect this process. If the number of electrodes is large, such as 10 pairs or 100 pairs, it will take more time for the electrodes to reach adsorption saturation. We will test the influence of the number of electrodes on the salt adsorption capacity and salt adsorption rate of the electrode in future work. The SAC of CBC-800 electrodes has no clear change during the five regeneration process, indicating CBC-800 electrodes possess a good regeneration performance and stability. This can be attributed to the following factors: (i) The mesopores can make the ion transport easier, and the micropores can provide more active adsorption sites; (ii) Heteroatoms doping can offer better electronic conductivity and good wettability, which is beneficial to the adsorption of ions. In a word, the high specific surface area, excellent meso/micropores structure and high content of nitrogen element of CBC-800 lead to its highest specific capacitance and smallest inner resistance, which predestines the best deionization and regeneration performance of CBC-800 electrodes.

Fig. 18 shows the charge efficiency (η) of CBC-800 electrodes at different NaCl solution concentrations and charging voltages. As shown in Fig. 18a, the charge efficiency of CBC-800 electrodes decreases from 71% to 60.3% when the charging voltage increases from 0.8 to 1.2 V, indicating the increase of the charging voltage is not conducive to the utilization of charge. A higher charging voltage

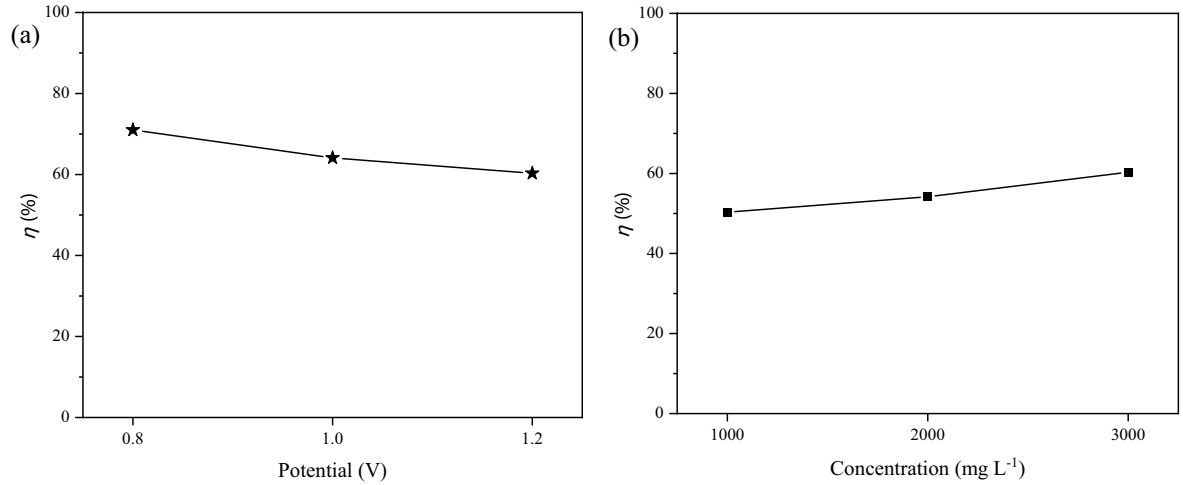


Fig. 18. (a) Plots of η vs. charging voltage for CBC-800 electrodes in a 3,000 mg·L$^{-1}$ NaCl solution. (b) Plots of η vs. solution concentration for CBC-800 electrodes at 1.2 V.

can provide more charge, but a large number of charges cannot be used efficiently. As shown in Fig. 18b, When the solution concentration increases from 1,000 to 3,000 mg·L$^{-1}$, the charge efficiency of CBC-800 electrodes increases from 50.3% to 60.3%. Apparently, the increase of solution concentration is beneficial to improve the charge efficiency. This can be attributed to the salt adsorption capacity of CBC-800 electrodes increases, which could consume more charge. The charge efficiencies of other electrodes in a 3,000 mg·L$^{-1}$ NaCl solution at 1.2 V are also shown in Figs. S10–S12. However, the value of the charge efficiency is always lower than 100%, which is mainly due to the following reasons: (i) the binder such as PTFE was used when preparing the electrode slurry, which would increase the inner resistance of the electrodes; (ii) the connection between the carbon materials and the nickel foam is not close enough, which would also waste a part of charge; (iii) the charge utilization decreases due to the common ion effect during the deionization process.

## 4. Conclusions

In a word, we successfully prepared the micro/mesoporous carbon materials derived from corncobs, cornstalks and waste cigarette butts through carbonization and chemical activation, and developed them as efficient electrodes for CDI desalination. The raw materials are cheap and easily available, and the preparation process is green and convenient. As a result, among the eight carbon materials made from three raw materials, the CBC-800 exhibits an excellent meso/microporous structure, the highest specific surface area of 1,201.90 m$^2$·g$^{-1}$ and the content of heteroatoms. The electrodes made from CBC-800 also possess a good electrochemical performance (the specific capacitance is 141.4 F·g$^{-1}$ at a scan rate of 5 mV·s$^{-1}$), high salt adsorption capacity (the value of SAC is 19.2 mg·g$^{-1}$ in a 3,000 mg·L$^{-1}$ NaCl solution), fast adsorption rate and good regeneration performance. Considering these above factors, compared with other carbon materials in this paper, the CBC-800 is a promising material for the desalination of salt water by CDI.

## Acknowledgements

This research was supported by the fund of National Natural Science Foundation of China under the contract No. 51676098. It was also supported by the grants from the fund of Natural Science Foundation of Jiangsu Province under the contract No. BK20160822. These supports are gratefully acknowledged.

## References

[1] R. Semiat, Energy issues in desalination processes, Environ. Sci. Technol., 42 (2008) 8193–8201.
[2] S.M. Montazeri, G. Kolliopoulos, Hydrate based desalination for sustainable water treatment: a review, Desalination, 537 (2022) 115855, doi: 10.1016/j.desal.2022.115855.
[3] R. Alrowais, M.W. Shahzad, M. Burhan, M.T. Bashir, Q. Chen, B.B. Xu, M. Kumja, C.N. Markides, K.C. Ng, A thermally-driven seawater desalination system: proof of concept and vision for future sustainability, Case Stud. Therm. Eng., 35 (2022) 102084, doi: 10.1016/j.csite.2022.102084.
[4] N.P.B. Tan, P.M.L. Ucab, G.C. Dadol, L.M. Jabile, I.N. Talili, M.T.I. Cabaraban, A review of desalination technologies and its impact in the Philippines, Desalination, 534 (2022) 115805, doi: 10.1016/j.desal.2022.115805.
[5] H. Xu, S. Jiang, M.X. Xie, T. Jia, Y.J. Dai, Technical improvements and perspectives on humidification-dehumidification desalination — a review, Desalination, 541 (2022) 116029, doi: 10.1016/j.desal.2022.116029.
[6] J. Zheng, F. Cheng, Y. Li, X. Lü, M. Yang, Progress and trends in hydrate-based desalination (HBD) technology: a review, Chin. J. Chem. Eng., 27 (2019) 2037–2043.
[7] D. Grey, D. Garrick, D. Blackmore, J. Kelman, M. Muller, C. Sadoff, Water security in one blue planet: twenty-first century policy challenges for science, Philos. Trans. R. Soc. London, Ser. A, 371 (2013) 0406, doi: 10.1098/rsta.2012.0406.
[8] UNESCO, Water Reuse Within a Circular Economy Context, United Nations Educational, Scientific and Cultural Organization (UNESCO), 2020.
[9] UNDESA, The United Nations Water Scarcity, International Decade for Action "Water For Life" 2005–2015, United Nations Department of Economic and Social Affairs (UNDESA), 2015.
[10] I. Prihatiningtyas, A.-H.A.H. Al-Kebsi, Y. Hartanto, T.M. Zewdie, B. Van der Bruggen, Techno-economic assessment of pervaporation desalination of hypersaline water, Desalination, 527 (2022) 115538, doi: 10.1016/j.desal.2021.115538.

[11] H. Zheng, General Problems in Seawater Desalination, In: Solar Energy Desalination Technology, 2017, pp. 1–46.
[12] H.T. El-Dessouky, H.M. Ettouney, Y. Al-Roumi, Multi-stage flash desalination: present and future outlook, Chem. Eng. J., 73 (1999) 173–190.
[13] B. Peñate, L. García-Rodríguez, Current trends and future prospects in the design of seawater reverse osmosis desalination technology, Desalination, 284 (2012) 1–8.
[14] N.I.H.A. Aziz, M.M. Hanafiah, Application of life cycle assessment for desalination: Progress, challenges and future directions, Environ. Pollut., 268 (2021) 115948, doi: 10.1016/j.envpol.2020.115948.
[15] J. Lee, K. Jo, J. Lee, S.P. Hong, S. Kim, J. Yoon, Rocking-chair capacitive deionization for continuous brackish water desalination, ACS Sustainable Chem. Eng., 6 (2018) 10815–10822.
[16] X. Chen, F. Jiang, Q. Jiang, Y. Jia, C. Liu, G. Liu, J. Xu, X. Duan, C. Zhu, G. Nie, P. Liu, Conductive and flexible PEDOT-decorated paper as high performance electrode fabricated by vapor phase polymerization for supercapacitor, Colloids Surf., A, 603 (2020) 126173, doi: 10.1016/j.colsurfa.2020.125173.
[17] Y. Yao, X.-h. Huang, B.-y. Zhang, Z. Zhang, D. Hou, Z.-k. Zhou, Facile fabrication of high sensitivity cellulose nanocrystals based QCM humidity sensors with asymmetric electrode structure, Sens. Actuators, B, 302 (2020) 127192, doi: 10.1016/j.snb.2019.127192.
[18] Y. Yang, Z. Shao, F. Wang, Preparation of Fe/N co-doped hierarchical porous carbon nanosheets derived from chitosan nanofibers for high-performance supercapacitors, J. Electrochem. Energy Convers. Storage, 19 (2021) 021009 (8 pages), doi: 10.1115/1.4052316.
[19] C.J. Linnartz, A. Rommerskirchen, M. Wessling, Y. Gendel, Flow-electrode capacitive deionization for double displacement reactions, ACS Sustainable Chem. Eng., 5 (2017) 3906–3912.
[20] S. Porada, R. Zhao, A. van der Wal, V. Presser, P.M. Biesheuvel, Review on the science and technology of water desalination by capacitive deionization, Prog. Mater. Sci., 58 (2013) 1388–1442.
[21] Y. Oren, Capacitive deionization (CDI) for desalination and water treatment — past, present and future (a review), Desalination, 228 (2008) 10–29.
[22] X. Gao, A. Omosebi, J. Landon, K. Liu, Surface charge enhanced carbon electrodes for stable and efficient capacitive deionization using inverted adsorption–desorption behavior, Energy Environ. Sci., 8 (2015) 897–909.
[23] A. Rommerskirchen, C.J. Linnartz, D. Müller, L.K. Willenberg, M. Wessling, Energy recovery and process design in continuous flow–electrode capacitive deionization processes, ACS Sustainable Chem. Eng., 6 (2018) 13007–13015.
[24] J. Kim, J. Kim, J.H. Kim, H.S. Park, Hierarchically open-porous nitrogen-incorporated carbon polyhedrons derived from metal-organic frameworks for improved CDI performance, Chem. Eng. J., 382 (2020) 122996, doi: 10.1016/j.cej.2019.122996.
[25] T. Yan, J. Liu, H. Lei, L. Shi, Z. An, H.S. Park, D. Zhang, Capacitive deionization of saline water using sandwich-like nitrogen-doped graphene composites *via* a self-assembling strategy, Environ. Sci.: Nano, 5 (2018) 2722–2730.
[26] X. Gong, S. Zhang, W. Luo, N. Guo, L. Wang, D. Jia, Z. Zhao, S. Feng, L. Jia, Enabling a large accessible surface area of a pore-designed hydrophilic carbon nanofiber fabric for ultrahigh capacitive deionization, ACS Appl. Mater. Interfaces, 12 (2020) 49586–49595.
[27] H.Y. Yang, Z.J. Han, S.F. Yu, K.L. Pey, K. Ostrikov, R. Karnik, Carbon nanotube membranes with ultrahigh specific adsorption capacity for water desalination and purification, Nat. Commun., 4 (2013) 2220, doi: 10.1038/ncomms3220.
[28] H. Zhang, F. Zhang, Y. Wei, Q. Miao, A. Li, Y. Zhao, Y. Yuan, N. Jin, G. Li, Controllable design and preparation of hollow carbon-based nanotubes for asymmetric supercapacitors and capacitive deionization, ACS Appl. Mater. Interfaces, 13 (2021) 21217–21230.
[29] C. Prehal, C. Koczwara, H. Amenitsch, V. Presser, O. Paris, Salt concentration and charging velocity determine ion charge storage mechanism in nanoporous supercapacitors, Nat. Commun., 9 (2018) 4145, doi: 10.1038/s41467-018-06612-4.
[30] M. Ding, S. Fan, S. Huang, M.E. Pam, L. Guo, Y. Shi, H.Y. Yang, Tunable pseudocapacitive behavior in metal–organic framework-derived $TiO_2$@porous carbon enabling high-performance membrane capacitive deionization, ACS Appl. Energy Mater., 2 (2019) 1812–1822.
[31] S. Wang, G. Wang, H. Song, S. Lv, T. Li, C. Li, *In-situ* formation of Prussian blue analogue nanoparticles decorated with three-dimensional carbon nanosheet networks for superior hybrid capacitive deionization performance, ACS Appl. Mater. Interfaces, 12 (2020) 44049–44057.
[32] X. Wen, M. Zhao, Z. Zhao, X. Ma, M. Ye, Hierarchical and self-supported vanadium disulfide microstructures@graphite paper: an advanced electrode for efficient and durable asymmetric capacitive deionization, ACS Sustainable Chem. Eng., 8 (2020) 7335–7342.
[33] D. Desai, E.S. Beh, S. Sahu, V. Vedharathinam, Q. van Overmeere, C.F. de Lannoy, A.P. Jose, A.R. Völkel, J.B. Rivest, Electrochemical desalination of seawater and hypersaline brines with coupled electricity storage, ACS Energy Lett., 3 (2018) 375–379.
[34] V.M. Rangaraj, A.A. Edathil, Y.Y. Kannangara, J.-K. Song, M.A. Haija, F. Banat, Tamarind shell derived N-doped carbon for capacitive deionization (CDI) studies, J. Electroanal. Chem., 848 (2019) 113307, doi: 10.1016/j.jelechem.2019.113307.
[35] M. Chu, W. Tian, J. Zhao, M. Zou, Z. Lu, D. Zhang, J. Jiang, A comprehensive review of capacitive deionization technology with biochar-based electrodes: biochar-based electrode preparation, deionization mechanism and applications, Chemosphere, 301 (2022) 136024, doi: 10.1016/j.chemosphere.2022.136024.
[36] Cigarette Butt Waste, America Nonsmokers' Rights Foundation [EB/OL], 2015.
[37] Q.Y. Dou, H.S. Park, Perspective on high-energy carbon-based supercapacitors, Energy Environ. Mater., 3 (2020) 286–305.
[38] J.S. Yeon, S.H. Park, J. Suk, H. Lee, H.S. Park, Confinement of sulfur in the micropores of honeycomb-like carbon derived from lignin for lithium-sulfur battery cathode, Chem. Eng. J., 382 (2020) 122946, doi: 10.1016/j.cej.2019.122946.
[39] H. Lei, T. Yan, H. Wang, L. Shi, J. Zhang, D. Zhang, Graphene-like carbon nanosheets prepared by a Fe-catalyzed glucose-blowing method for capacitive deionization, J. Mater. Chem. A, 3 (2015) 5934–5941.
[40] W. Qian, F. Sun, Y. Xu, L. Qiu, C. Liu, S. Wang, F. Yan, Human hair-derived carbon flakes for electrochemical supercapacitors, Energy Environ. Sci., 7 (2014) 379–386.
[41] L. Chang, J. Li, X. Duan, W. Liu, Porous carbon derived from metal–organic framework (MOF) for capacitive deionization electrode, Electrochim. Acta, 176 (2015) 956–964.
[42] Y. Liu, L. Pan, T. Chen, X. Xu, T. Lu, Z. Sun, D.H.C. Chua, Porous carbon spheres via microwave-assisted synthesis for capacitive deionization, Electrochim. Acta, 151 (2015) 489–496.
[43] J. Wang, S. Kaskel, KOH activation of carbon-based materials for energy storage, J. Mater. Chem., 22 (2012) 23710–23725.
[44] M. Thommes, K. Kaneko, A.V. Neimark, J.P. Olivier, F. Rodriguez-Reinoso, J. Rouquerol, K.S.W. Sing, Physisorption of gases, with special reference to the evaluation of surface area and pore size distribution (IUPAC Technical Report), Pure Appl. Chem., 87 (2015) 1051–1069.
[45] J. Zhang, X. Zhang, Y. Zhou, S. Guo, K. Wang, Z. Liang, Q. Xu, Nitrogen-doped hierarchical porous carbon nano-whisker ensembles on carbon nanofiber for high-performance supercapacitors, ACS Sustainable Chem. Eng., 2 (2014) 1525–1533.
[46] M.S. Zoromba, M.H. Abdel-Aziz, M. Bassyouni, S. Gutub, D. Demko, A. Abdelkader, Electrochemical activation of graphene at low temperature: the synthesis of three-dimensional nanoarchitectures for high performance supercapacitors and capacitive deionization, ACS Sustainable Chem. Eng., 5 (2017) 4573–4581.
[47] L. Hao, X. Li, L. Zhi, Carbonaceous electrode materials for supercapacitors, Adv. Mater., 25 (2013) 3899–3904.
[48] G. Zheng, L. Hu, H. Wu, X. Xie, Y. Cui, Paper supercapacitors by a solvent-free drawing method, Energy Environ. Sci., 4 (2011) 3368–3373.

[49] C. Zhao, G. Liu, N. Sun, X. Zhang, G. Wang, Y. Zhang, H. Zhang, H. Zhao, Biomass-derived N-doped porous carbon as electrode materials for Zn-air battery powered capacitive deionization, Chem. Eng. J., 334 (2018) 1270–1280.
[50] B. Xu, F. Wu, R. Chen, G. Cao, S. Chen, G. Wang, Y. Yang, Room temperature molten salt as electrolyte for carbon nanotube-based electric double layer capacitors, J. Power Sources, 158 (2006) 773–778.
[51] R.K. Sharma, H.-S. Oh, Y.-G. Shul, H. Kim, Growth and characterization of carbon-supported $MnO_2$ nanorods for supercapacitor electrode, Physica B, 403 (2008) 1763–1769.
[52] L. Mao, H.S.O. Chan, J. Wu, Cetyltrimethylammonium bromide intercalated graphene/polypyrrole nanowire composites for high performance supercapacitor electrode, RSC Adv., 2 (2012) 10610–10617.
[53] A. Bello, F. Barzegar, D. Momodu, J. Dangbegnon, F. Taghizadeh, N. Manyala, Symmetric supercapacitors based on porous 3D interconnected carbon framework, Electrochim. Acta, 151 (2015) 386–392.
[54] D. Zhang, T. Yan, L. Shi, Z. Peng, X. Wen, J. Zhang, Enhanced capacitive deionization performance of graphene/carbon nanotube composites, J. Mater. Chem., 22 (2012) 14696–14704.
[55] K.T. Cho, S.B. Lee, J.W. Lee, Facile synthesis of highly electrocapacitive nitrogen-doped graphitic porous carbons, J. Phys. Chem. C, 118 (2014) 9357–9367.
[56] K.-B. Li, D.-W. Shi, Z.-Y. Cai, G.-L. Zhang, Q.-A. Huang, D. Liu, C.-P. Yang, Studies on the equivalent serial resistance of carbon supercapacitor, Electrochim. Acta, 174 (2015) 596–600.
[57] Z. Chen, C. Song, X. Sun, H. Guo, G. Zhu, Kinetic and isotherm studies on the electrosorption of NaCl from aqueous solutions by activated carbon electrodes, Desalination, 267 (2011) 239–243.

## Supporting information

### S1. Introduction

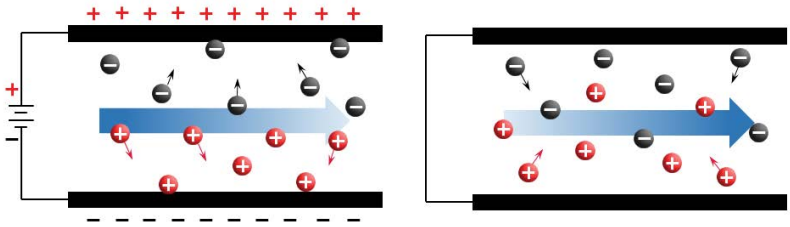

Fig. S1. Schematic diagram of capacitive deionization.

### S2. Materials and methods

*Deionization experiments*

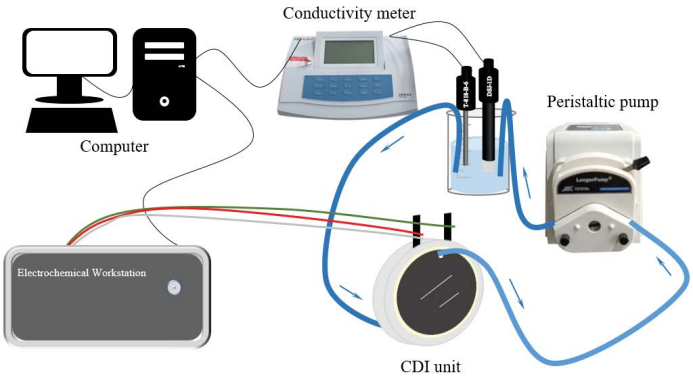


Fig. S2. Schematic illustration of CDI desalination experiment.

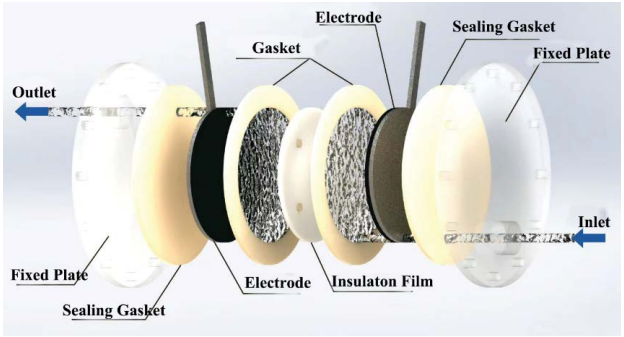


Fig. S3. Schematic diagram of CDI cell structure.

## S3. Results and discussion

*Characteristics*

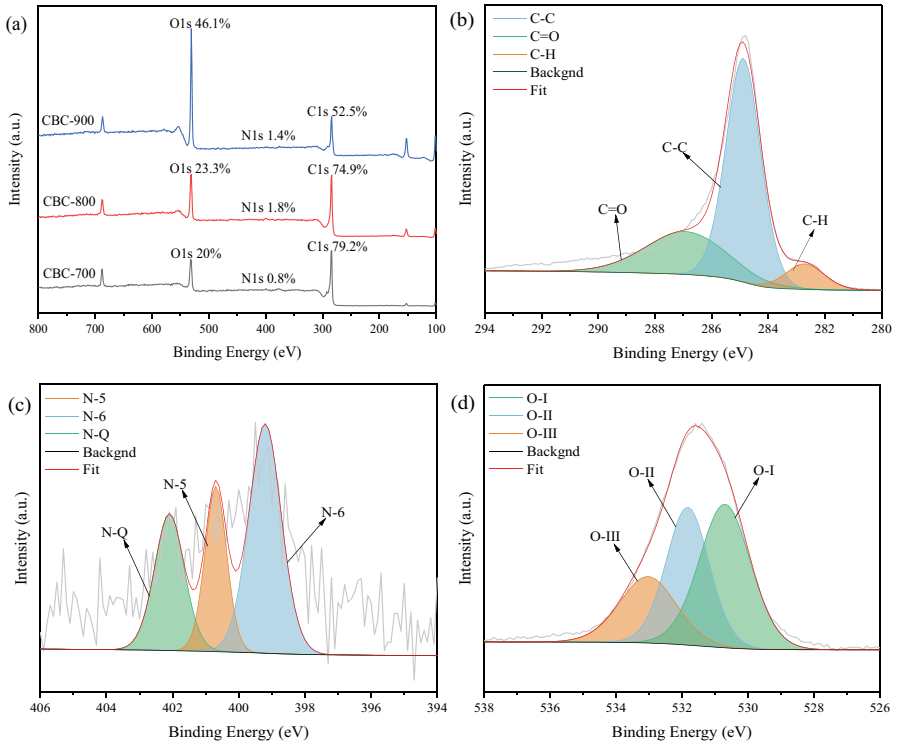


Fig. S4. XPS results of CBC-X.

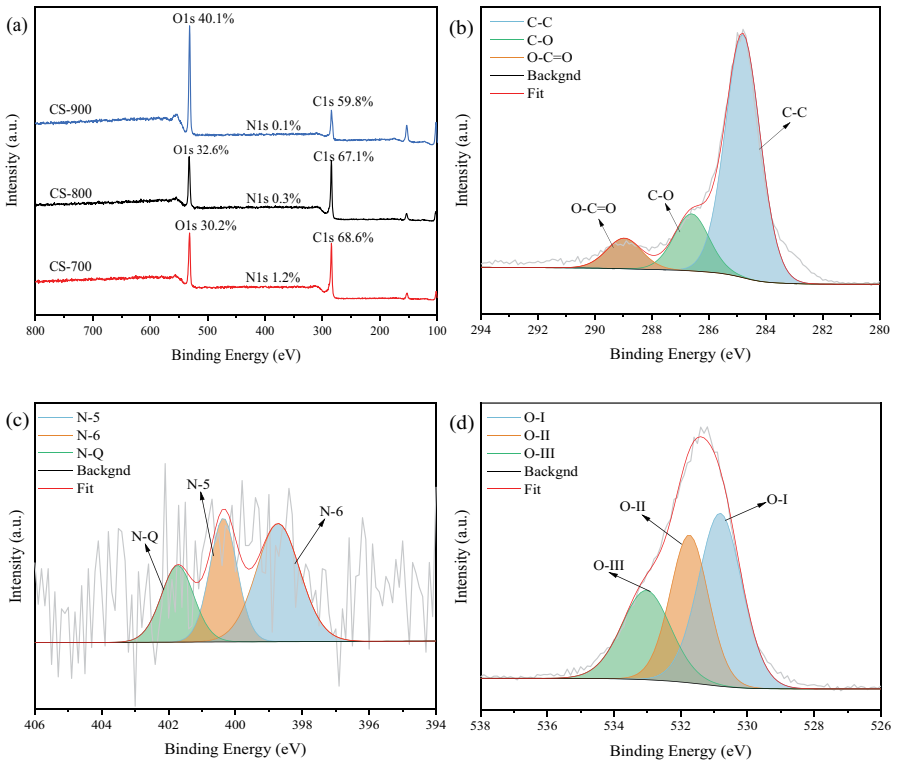


Fig. S5. XPS results of CS-X.

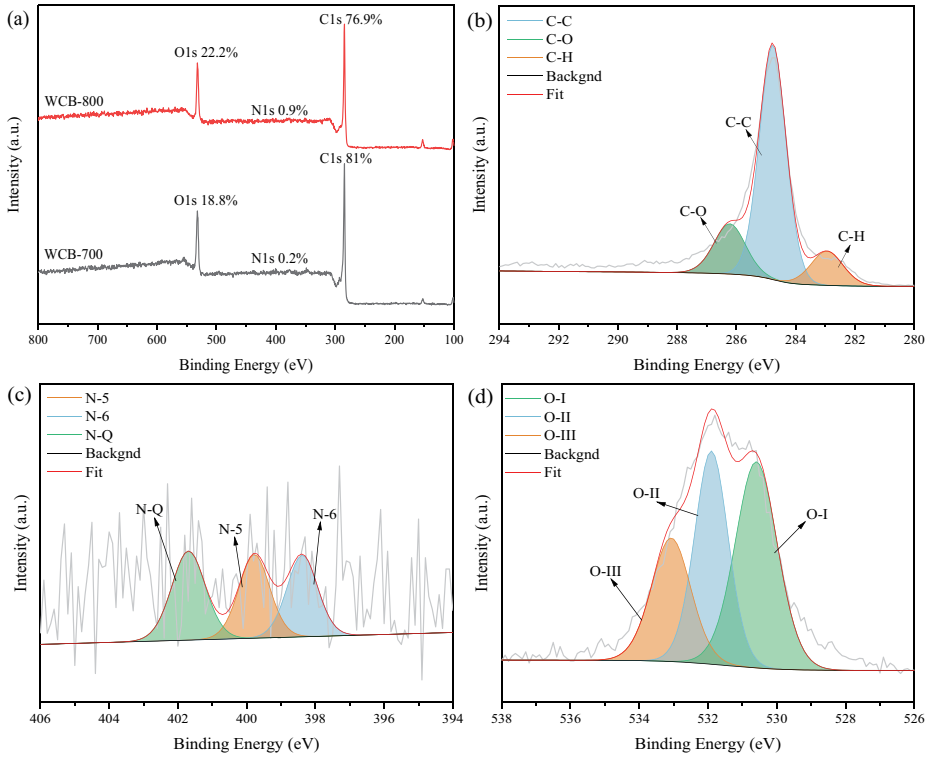


Fig. S6. XPS results of WCB-X.

*Electrochemical performance*

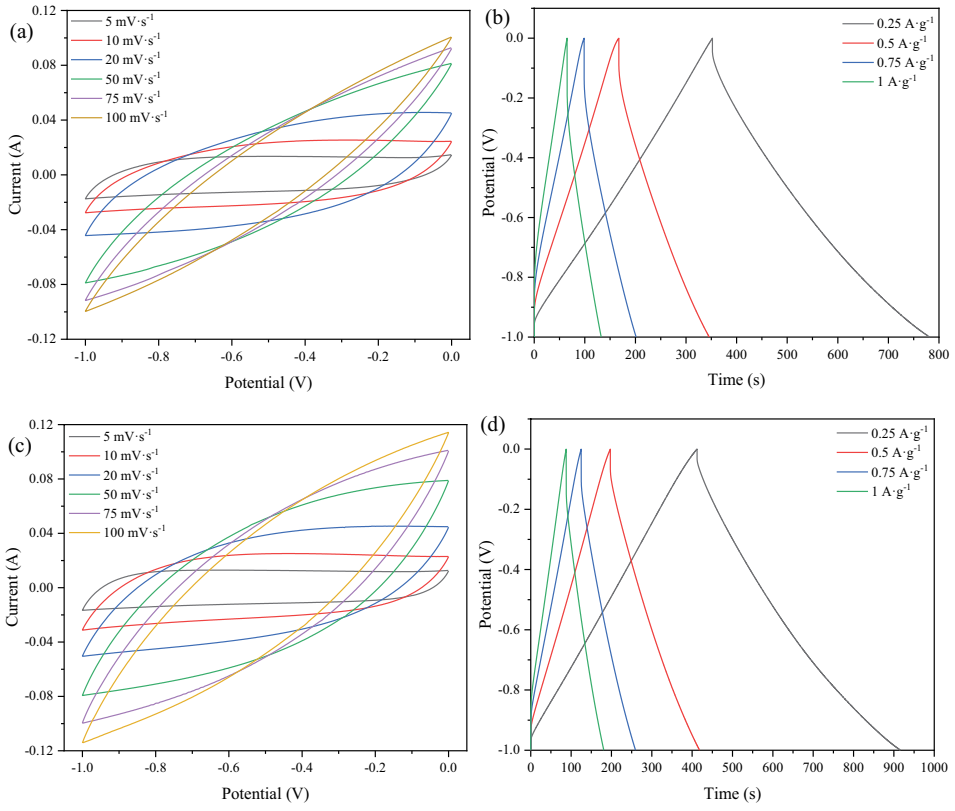


*Fig. S7 (Continued)*

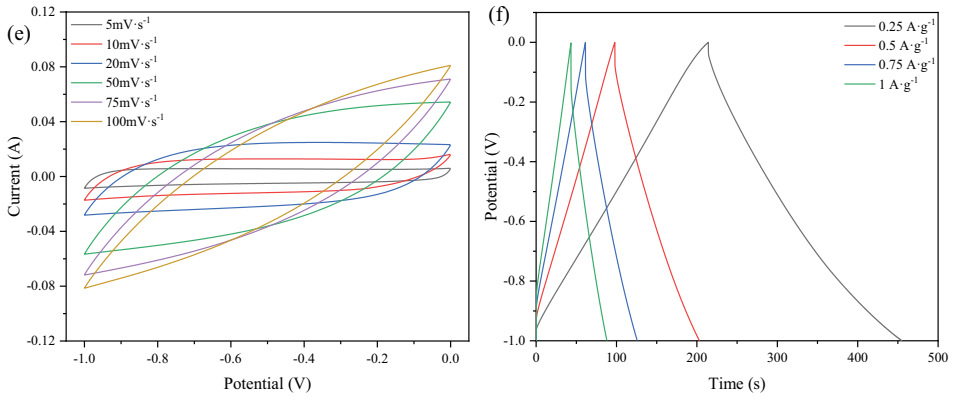


Fig. S7. (a) CV curves and (b) GCD curves of the CBC-700 electrodes. (c) CV curves and (d) GCD curves of the CBC-800 electrodes. (e) CV curves and (f) GCD curves of the CBC-900 electrodes. The solution is 1 M NaCl solution.

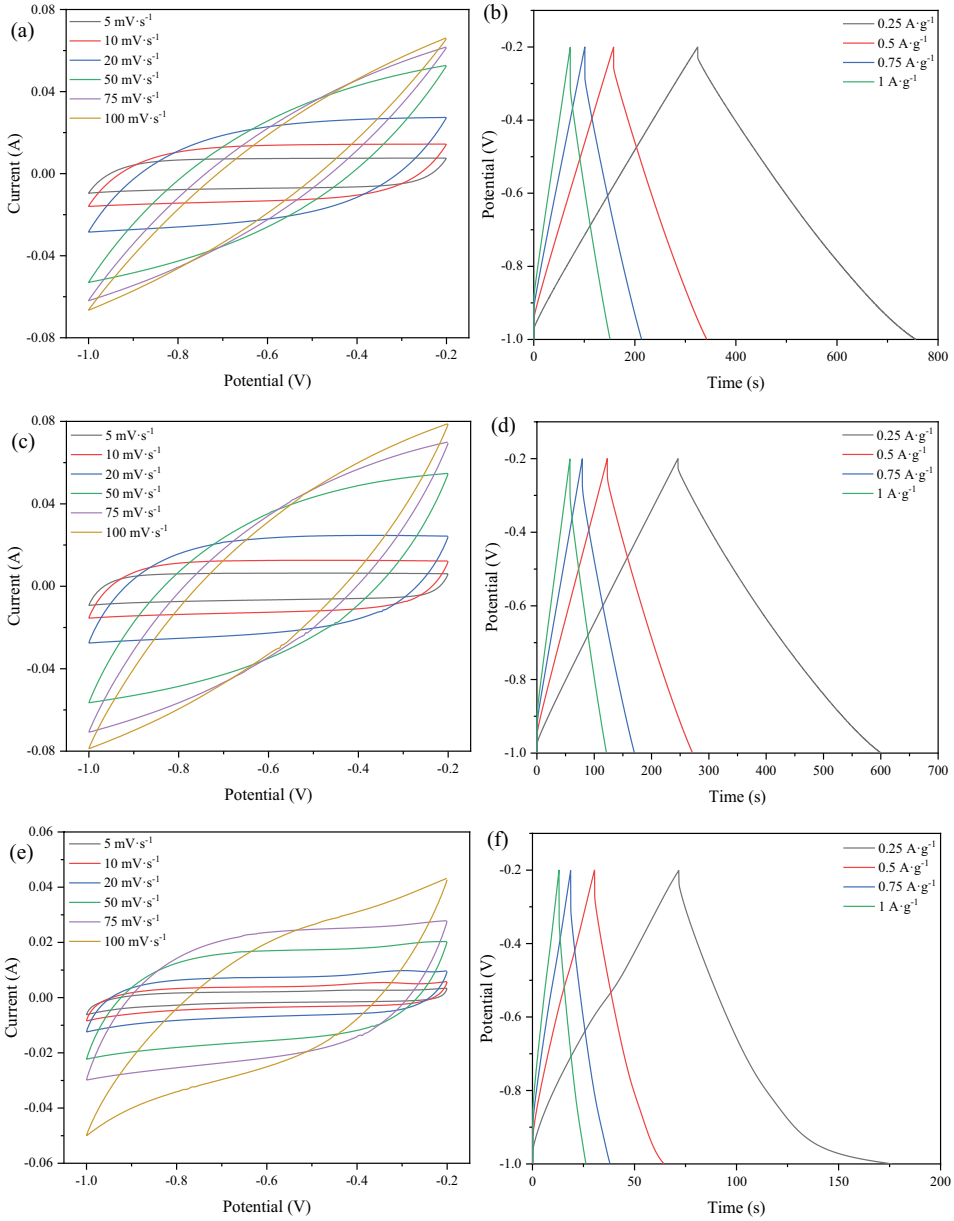


Fig. S8. (a) CV curves and (b) GCD curves of the CS-700 electrodes. (c) CV curves and (d) GCD curves of the CS-800 electrodes. (e) CV curves and (f) GCD curves of the CS-900 electrodes. The solution is 1 M NaCl solution.

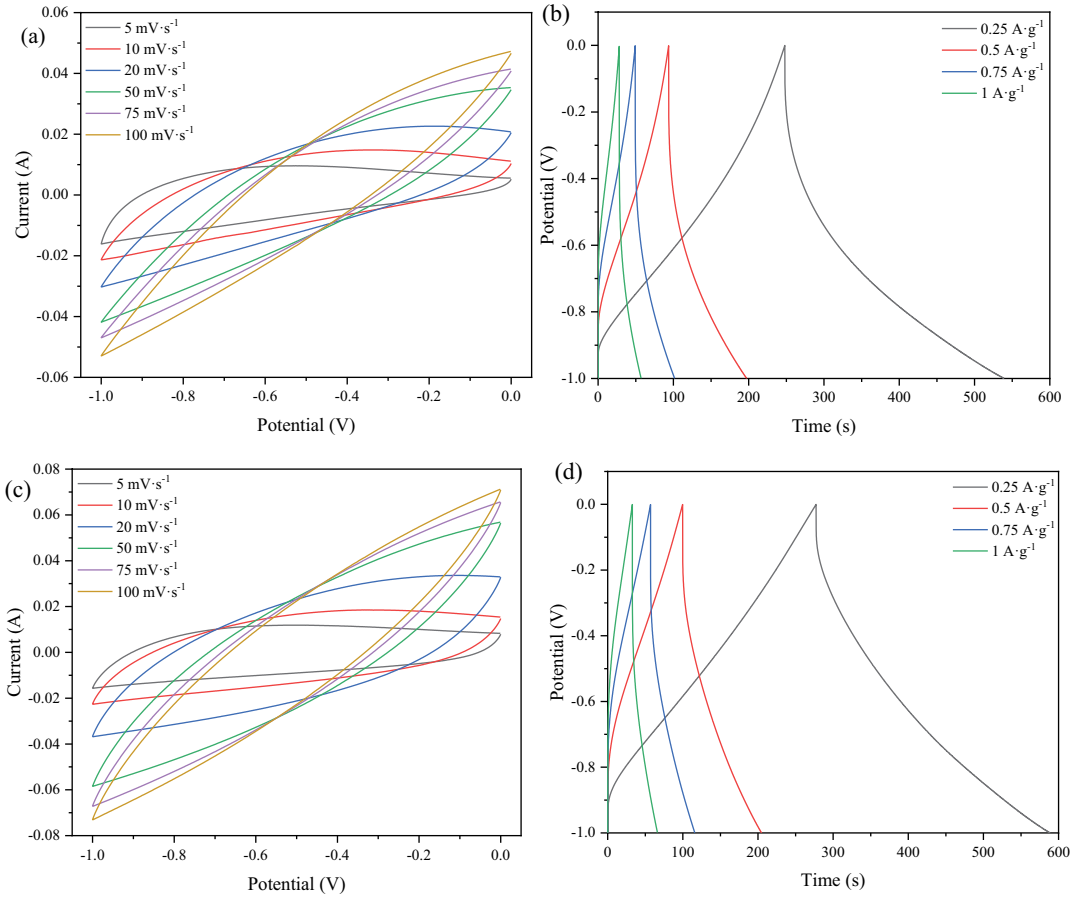


Fig. S9. (a) CV curves and (b) GCD curves of the WCB-700 electrodes. (c) CV curves and (d) GCD curves of the WCB-800 electrodes. The solution is 1 M NaCl solution.

*Deionization performance*

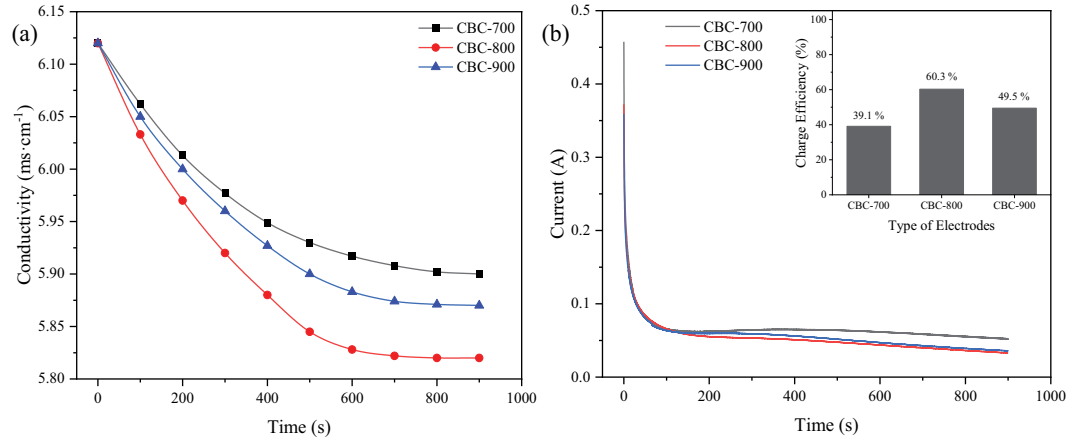


Fig. S10. (a) Plots of conductivity vs. time and (b) current transient curves and charge efficiency for CBC electrodes in a 3,000 mg·L$^{-1}$ NaCl solution at 1.2 V.

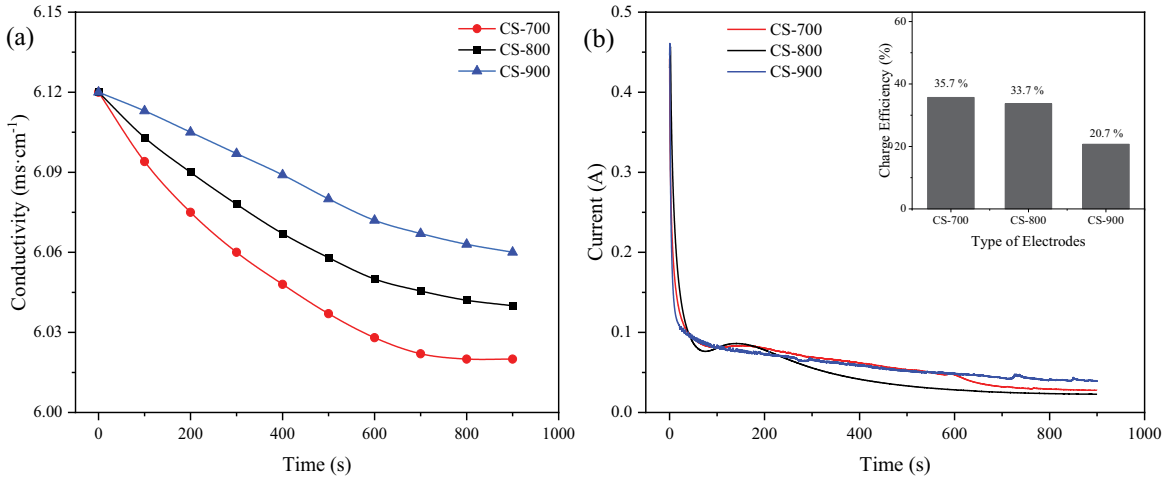


Fig. S11. (a) Plots of conductivity vs. time and (b) current transient curves and charge efficiency for CS electrodes in a 3,000 mg·L$^{-1}$ NaCl solution at 1.2 V.

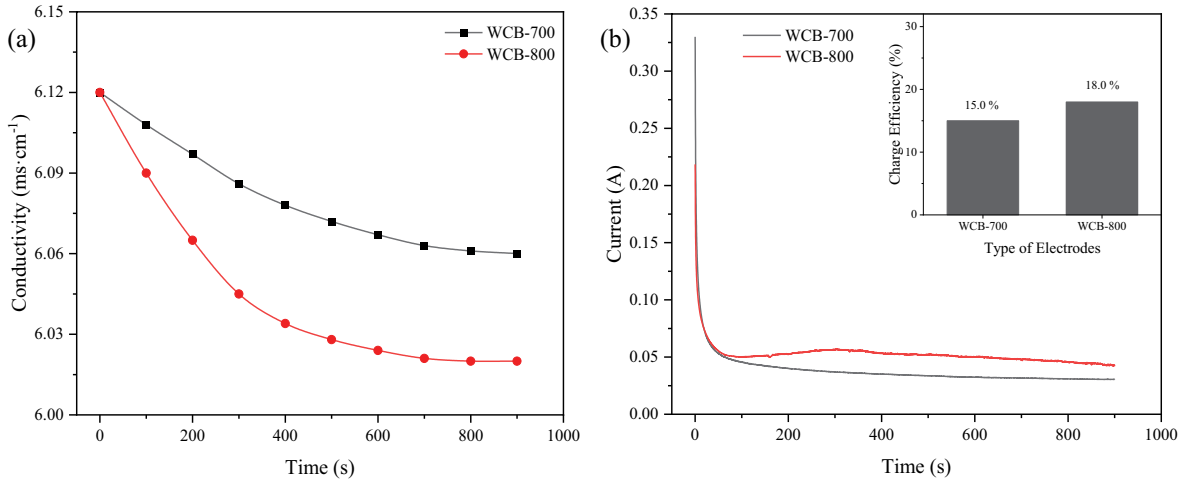


Fig. S12. (a) Plots of conductivity vs. time and (b) current transient curves and charge efficiency for WCB electrodes in a 3,000 mg·L$^{-1}$ NaCl solution at 1.2 V.